Chapter 8

Cosmic Rays: Physics, Chemistry, and Computational Challenges

Marco Padovani[1], *Brandt Gaches*[2,3,4]

[1]*INAF Osservatorio Astrofisico di Arcetri, Largo E. Fermi 5, 50125 Firenze, Italy,*
[2]*I. Physikalisches Institut, Universität zu Köln, Zülpicher Straße 77, 50937, Köln, Germany,*
[3]*Department of Space, Earth and Environment, Chalmers University of Technology, Gothenburg SE-412 96, Sweden,*
[4]*Center of Planetary Systems Habitability, The University of Texas at Austin, USA*

ABSTRACT

In regions shielded from ultraviolet radiation, energetic charged particles, called cosmic rays, are the dominant drivers of ionization, dissociation, and excitation. This chapter discusses the basics of cosmic-ray transport and acceleration, their impact on the thermochemistry of molecular gas, and methods to include cosmic-ray processes into astrochemical models.

KEYWORDS

cosmic rays, atomic and molecular processes, interstellar medium, high-energy processes

The interstellar medium is immersed in a bath of cosmic rays: energetic charged particles with a non-thermal velocity distribution that exist in rough equipartition with the thermal and magnetic energies. Observations have shown that cosmic rays follow power-law distributions in energy from 1 GeV to 10 EeV with a turnover around 1 GeV. Cosmic rays are thought to have a wide range of effects on the interstellar medium and galaxies, such as ionization and heating of gas, pressure which aids in lifting gas out of galaxies, producing turbulence through instabilities in magneto-hydrodynamic turbulence. In this chapter, we will focus on the first of these and refer the reader to the many excellent reviews of the later effects (e.g., Strong et al. 2007; Zweibel 2013; Grenier et al. 2015; Schlickeiser 2015). We also refer the reader to Schlickeiser (2002) and Longair (2011) for more thorough monographs on cosmic-ray transport and high-energy phenomenon.

Cosmic-ray astrochemistry leaves radiative fingerprints across the electromagnetic spectrum, as highlighted in Fig. 8.1. The molecular chemistry cosmic

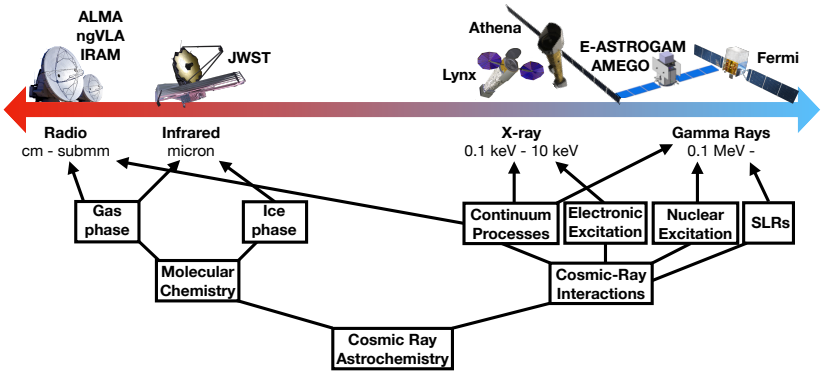

FIGURE 8.1 Emission processes diagnostics of cosmic-ray astrochemistry, with key current and proposed/future telescopes denoted at their respective wavelength regimes.

rays induced appear in emission and absorption lines from radio to infrared wavelengths (Sect. 8.1). Interactions of cosmic rays with dense gas produce both continuum emission, such as gamma-ray and non-thermal radio emission, and line emission resulting from nuclear interactions. As such, the study of cosmic-ray astrochemistry involves investigations of radiation across the entire electromagnetic spectrum, and coupling physical processes from high-energy astrophysics, particle physics, and chemistry.

Cosmic rays differ from radiation in that they do not travel directly to Earth from their sources, but spread across the Galaxy due to their interactions with magnetic fields. As such, observations of cosmic rays are representative of the population of particles accelerated throughout the Galaxy that are now flowing across our neighborhood.

Cosmic-ray particles comprise electrons, protons, and heavy nuclei. The electronic component can be estimated by observations of Galactic synchrotron emission, which depends on the strength of the interstellar magnetic field (e.g., Ginzburg & Syrovatskii 1965; Girart et al. 2009; Orlando 2018; Padovani & Galli 2018; Padovani et al. 2021a). The latter is independently estimated using other methods, e.g., modeling the polarized thermal emission of dust (e.g., Alves et al. 2018; Beltrán et al. 2019; Sanhueza et al. 2021), from Zeeman splitting of hyperfine molecular transitions (e.g., Crutcher et al. 1996), optical and near-infrared polarization of starlight (e.g., Alves et al. 2008, 2011), maser emission polarization (e.g., Vlemmings et al. 2011), Faraday rotation (e.g., Wolleben & Reich 2004; Bracco et al. 2022), and Goldreich–Kylafis effect (e.g., Goldreich & Kylafis 1981). The proton component of cosmic rays above about 1 GeV is constrained by local γ-ray emissivity observations (Casandjian 2015; Strong & Fermi-LAT Collaboration 2015; Orlando 2018). However, results depend on the cosmic-ray propagation and solar modulation models that are assumed (see Tibaldo et al. 2021 for a review). At lower energies, between about 3 and 300

Species k	C	E_0 [MeV]	α	$\beta - \alpha$
e^-	2.1(18)	710	−1.3	3.2
p (model $\mathscr{L}$)	2.4(15)	650	0.1	2.7
p (model $\mathscr{H}$)	2.4(15)	650	−0.8	2.7

TABLE 8.1 Parameters of the interstellar CR electron (e^-) and proton (p) spectra, Eq. (8.1), where E is in MeV and C is in units of eV^{-1} s^{-1} cm^{-2} sr^{-1}. Numbers in brackets indicate the power of ten, i.e. $a(b) = a \times 10^b$.

MeV, local interstellar cosmic rays, including heavy species, are estimated by measurements obtained from the two Voyager spacecraft (Cummings et al. 2016; Stone et al. 2019). Nevertheless, the magnetic field direction measured by the Voyager probes does not show the change expected if the spacecraft would not have been influenced by solar modulation (Gloeckler & Fisk 2015). Moreover, fluctuations in the cosmic-ray spectrum throughout the Galaxy could be present due to the discrete nature of cosmic-ray sources (Phan et al. 2021). As a result, there is significant uncertainty about the low-energy cosmic-ray spectrum.

The cosmic-ray spectrum, also known as cosmic-ray flux, $j(E)$, is the number of particles per unit energy, area, time, and solid angle. It is usually parameterized by

$$j_k^{\rm IS}(E) = C \frac{E^\alpha}{(E + E_0)^\beta} \ {\rm eV}^{-1} \ {\rm s}^{-1} \ {\rm cm}^{-2} \ {\rm sr}^{-1} \,, \tag{8.1}$$

where $k = e, p$ are electrons and protons, respectively. The adopted values of the parameters C, E_0, α, and β are listed in Tab. 8.1.

While at energies above about 1-10 GeV the cosmic-ray proton and electron spectra are well constrained by observations with instruments such as AMS-02, *Fermi*-LAT, and Pamela, at lower energies only recently, the Voyager probes have provided information on the bending of the spectrum (see Fig. 8.2). At present, there remains significant uncertainty about how representative the Voyager measurements are of the interstellar spectrum. Presumably, the data collected by the probes, which are currently located about 156 au (Voyager 1) and 130 au (Voyager 2) from the Sun[1], are representative only of the spectrum in the solar surroundings. As described in Sect. 8.1.1, the quintessential quantity that gives information about the trend of the cosmic-ray spectrum at low energies is the ionization rate, namely the number of ionizations of atomic or molecular hydrogen per unit time. Using a spectrum that reproduces the Voyager data (*low* model $\mathscr{L}$ with $\alpha = 0.1$ in Fig. 8.2), one obtains only a lower limit to the estimates of the ionization rate in diffuse clouds (see Fig. 8.4). This is why different parameterizations of the spectrum are commonly used at low energies, in particular for cosmic-ray protons. In addition to the model $\mathscr{L}$, Fig. 8.2 displays the *high* spectrum $\mathscr{H}$, with $\alpha = -0.8$, which better describes the average value of the cosmic-ray ionization rate estimated in diffuse clouds (see Sect. 8.1.1), and an extreme case with $\alpha = -1.2$, whose corresponding ionization rate trend

1. https://voyager.jpl.nasa.gov/mission/status/

follows the upper envelope of values in diffuse clouds (see Fig. 8.4). Since the contribution of cosmic-ray protons to the ionization of the medium dominates in most cases, indicatively for $\alpha \gtrsim -0.4$ and H_2 column densities larger than about 10^{21} cm^{-2}, a single parameterization for primary cosmic-ray electrons is usually considered (see right panel of Fig. 8.2).

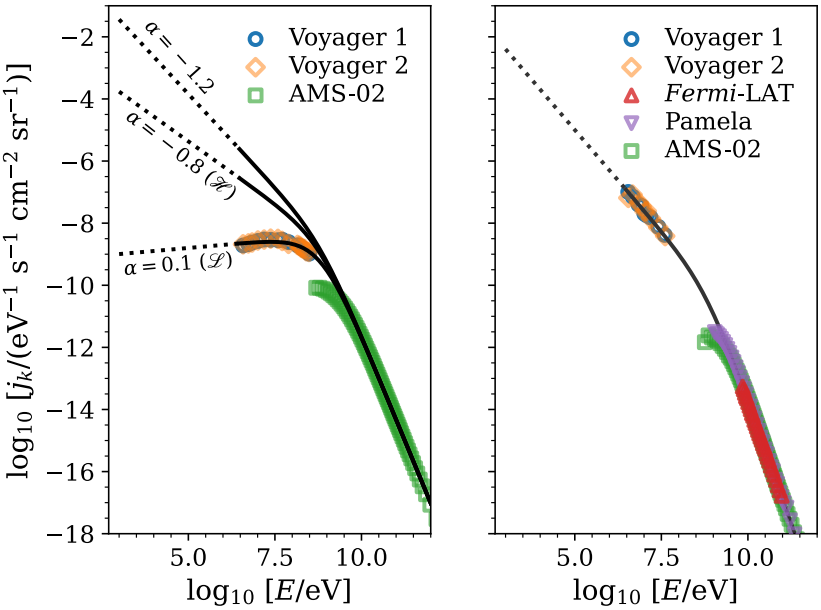

FIGURE 8.2 Galactic cosmic-ray proton and electron spectra. Left panel: cosmic-ray proton spectrum as a function of the energy for three low-energy spectral slopes: $\alpha = 0.1$ (labelled as model $\mathscr{L}$), $\alpha = -0.8$ (labelled as model $\mathscr{H}$), and $\alpha = -1.2$. Right panel: cosmic-ray electron spectrum as a function of the energy. Data are from Voyager 1 (blue circles; Cummings et al. 2016); Voyager 2 (orange diamonds; Stone et al. 2019); Fermi-LAT (upward-pointing red triangles; Ackermann et al. 2010); Pamela (downward-pointing purple triangles; Adriani et al. 2011); and AMS-02 (green squares; Aguilar et al. 2014, 2015).

8.1 COSMIC-RAY CHEMISTRY AND ITS DIAGNOSTIC IMPORTANCE

Low-energy cosmic rays, particularly those with energies below 1 GeV, drive the thermochemistry of shielded molecular gas. Due to the cold temperatures and low densities, much of the interstellar molecular chemistry goes through two-body ion-neutral reactions. The cosmic-ray-initiated chemistry stems from the ionization of both atomic and molecular hydrogen. In particular, following the ionization of H_2 to H_2^+, the H_2^+ rapidly interacts with nascent H_2 to form the trihydrogen cation H_3^+. From this, a wide range of proton-transfer reactions

can occur following

$$H_3^+ + X \rightarrow XH^+ + H_2 \,.$$

Many observationally important molecules are formed this way, such as HCO^+ and N_2H^+. Similarly, water formation can occur through the interaction of H_3^+ with O:

$$\begin{aligned} H_3^+ + O &\rightarrow OH^+ + H_2 \\ OH^+ + H_2 &\rightarrow H_2O^+ + H \\ H_2O^+ + H_2 &\rightarrow H_3O^+ + H \\ H_3O^+ + e^- &\rightarrow H_2O + H \,. \end{aligned}$$

It is worth noting that this chain can be initiated in warmer gas with a low molecular fraction through the following cosmic-ray-initiated chain

$$\begin{aligned} H + CR &\rightarrow H^+ + e^- + CR' \\ H^+ + O + \Delta E &\rightleftharpoons O^+ + H \\ O^+ + H_2 &\rightarrow OH^+ + H \,, \end{aligned}$$

where CR′ is the initial cosmic ray with reduced energy and $\Delta E = 226$ K is the endothermicity of the forward reaction (Indriolo et al. 2015). Through similar reaction chains involving H_2, hydrocarbons can be built following $H_3^+ + C$,

$$\begin{aligned} H_3^+ + C &\rightarrow CH^+ + H_2 \\ CH^+ + H_2 &\rightarrow CH_2^+ + H \\ &\ldots \\ CH_n^+ + H_2 &\rightarrow CH_{n+1}^+ + H \,. \end{aligned}$$

These species can lead to the formation of hydrogenated carbon chain species. Finally, the deuteration process occurs similarly as above, with the formation of H_2D^+ through HD and subsequent deuterium exchange reactions, e.g.,

$$H_2D^+ + N_2 \rightarrow N_2D^+ + H_2 \,.$$

Cosmic rays can also be important sources of destruction for molecules. For example, He^+, formed through the ionization of nascent neutral H_2, is a prominent destroyer of molecules, in particular of CO in dense gas, as

$$CO + He^+ \rightarrow C^+ + O + He \,.$$

While other atoms are also ionized through cosmic-ray interactions, due to their reduced abundance compared to hydrogen and helium, their ionization is not as significant of a driver. Fig. 8.3 shows a brief overview of the chemical diversity initiated through cosmic-ray ionization processes, and the resulting explosion of ion-neutral chemistry (often ending in recombinations to neutrals).

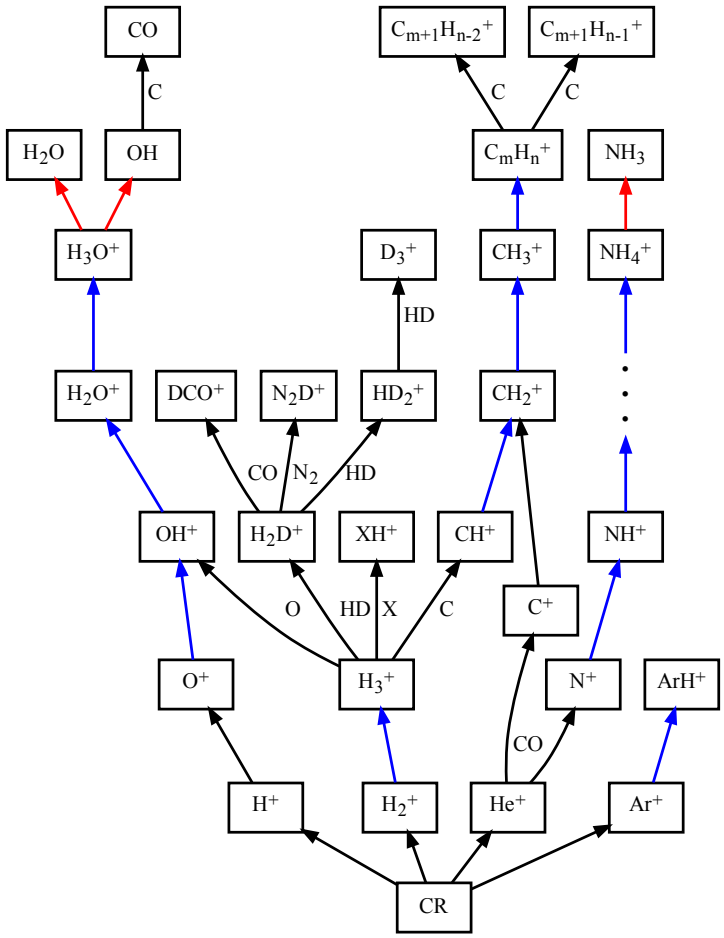

FIGURE 8.3 The *cosmic-ray chemistry tree*. Blue lines indicate H_2 interactions, and red lines e^- recombination. XH^+ refers to ions produced through the proton transfer reaction, such as N_2H^+ and HCO^+ from N_2 and CO, respectively (represented by X). The dots after NH^+ represent hydrogen abstraction reactions with H_2 (e.g., $NH^+ + H_2 \rightarrow NH_2^+ + H$).

The ionization of H_2 by cosmic rays is quantified through the cosmic-ray ionization rate, ζ_{H_2}, namely the number of ionization of hydrogen molecule per unit

time,

$$\zeta_{\mathrm{H_2}} = \int \mathrm{d}\Omega \left\{ \sum_k \int_{I(\mathrm{H_2})} j_k(E_k)[1+\phi_k(E_k)]\sigma_k^{\mathrm{ion}}(E_k)\mathrm{d}E_k + \int_0 j_p(E_p)\sigma_p^{\mathrm{e.c.}}(E_p)\mathrm{d}E_p \right\}, \tag{8.2}$$

where k refers to the primary cosmic-ray species (protons and electrons), j_k is the cosmic-ray spectrum (see Sect. 7.5), σ_k^{ion} and $\sigma_p^{\mathrm{e.c.}}$ are the ionization cross sections and the electron capture cross section by proton impact (see Tab. 8.4 and Tab. 8.5). Here, ϕ_k is a correction factor accounting for the ionization of H_2 by secondary electrons, whose commonly adopted value is 0.67 (Dalgarno & Griffing 1958). We note that Ivlev et al. (2021); Padovani et al. (2022) showed that ϕ_k is column-density dependent and spans between 0.7 and 1.1 and between 1.3 and 1.8 for protons and electrons, respectively, for column densities in the range $10^{20}-10^{23}$ cm^{-2}. While Eq. (8.2) is written specifically for H_2, it applies to any species given the appropriate ionization and electron capture cross sections.

SUGGESTION 8.1

Special attention must be paid to the notation used for the ionization rate. In particular, $\zeta_{\mathrm{H_2}}$, the ionization rate of molecular hydrogen due to cosmic rays and energetic secondary electrons produced via ionization, is sometimes labelled as ζ_2. The ionization rate of atomic hydrogen due to cosmic rays and energetic secondary electrons produced via ionization is marked by ζ_{H} and occasionally by ζ_1. Finally, the ionization rate of atomic hydrogen due only to cosmic-ray particles is denoted by ζ_p. The following relations apply: $\zeta_{\mathrm{H}} = 1.5\zeta_p$ and $\zeta_{\mathrm{H_2}} = 2.3\zeta_p$ (Glassgold & Langer 1974)

The cosmic-ray ionization rate of a particular species i, ζ_i, is typically scaled with that of H_2, i.e., $\zeta_i = k_0\zeta_{\mathrm{H_2}}$. The conversion factor k_0 accounts for differences in the ionization cross sections and ionization due to secondary electrons. Cosmic rays are included into chemical networks by adding the corresponding destruction/creation terms to the chemical network equation through unimolecular reactions, where $k_i = \zeta_i$. Tab. 8.2 lists commonly included gas-phase cosmic-ray ionization reactions and their scaling factors, k_0. We note that these coefficients are sometimes approximated, and a spectrum-resolved, or cosmic-ray species-dependent treatment is still not included in any public astrochemistry code. The scaling factors in Tab. 8.2 are primarily taken from Black (1975). For these, the ionization rates for hydrogen and helium species are based on data later presented in Cravens et al. (1975) and Cravens & Dalgarno (1978), while the rest are computed by scaling the high-energy cross sections by the electron charge number and electron binding energy (see e.g., Garcia et al. 1968; Welsheit 1973).

	Reaction	k_0	Reference
Cosmic-Ray Ionization	H + CR → H^+ + e^-	4.6(-1)	1
	He + CR → He^+ + e^-	5(-1)	1
	C + CR → C^+ + e^-	1.77	2
	N + CR → N^+ + e^-	2.1	1
	O + CR → O^+ + e^-	2.8	1
	Ar + H → Ar^+ + e^-	10 + 3.85ϕ	3
	CO + CR → C + O	5.0	1
	CO + CR → CO^+ + e^-	3.0	1
	N_2 + CR → N + N	p	1
	H_2 + CR → H + H	1.0(-1)	1
		6.0(-1) - 7.0(-1)	4
	H_2 + CR → H + H^+ + e^-	2.2(-2)	1
	H_2 + CR → H^+ + H^-	3(-4)	1
	H_2 + CR → H_2^+ + e^-	9.3(-1)	1
Cosmic-Ray Photon	C + CRP → C^+ + e^-	2.6(2)	5
	N + CRP → N^+ + e^-	7.34(-1)	1
	O + CRP → O^+ + e^-	2.7	5
	Si + CRP → Si^+ + e^-	4.2(3)	5
	CO + CRP → C + O	4.6(1)	5
	OH + CRP → O + H	4.70(2)	5
	O_2 + CRP → O + O	7.80(2)	5
	SiO + CRP → Si + O	8.90(2)	5
	H_2O + CRP	1.00(3)	5
	H_2O + CRP → H + OH	7.6(2)	1
	H_2O + CRP → O + H_2	2.2(2)	1

TABLE 8.2 Representative cosmic-ray ionization chemical reactions and their reaction scaling factors, such that the rate of each reaction is $k_i = k_0\zeta_{H_2}$. In the C_i column, terms given in parentheses denotes exponents, i.e. $a(b) = a \times 10^b$. For brevity, we drop the cosmic ray from the products of each reaction. The UMIST scaling factors for cosmic-ray ionization were derived by dividing their given rates by $\zeta_c = 1.3 \times 10^{-17}$ s^{-1}. References: 1 (KIDA, Wakelam et al. 2015), 2 (UMIST12, McElroy et al. 2013), 3 (Schilke et al. 2014), 4 (Padovani et al. 2018a), 5 (Heays et al. 2017). The cosmic-ray ionization reactions from UMIST were originally presented in Black (1975).

8.1.1 Constraining the cosmic-ray ionization rate

There have been several observational surveys to constrain the cosmic-ray ionization rate (Caselli et al. 1998; van der Tak & van Dishoeck 2000; McCall et al. 2002; Indriolo & McCall 2012; Indriolo et al. 2015; Neufeld & Wolfire 2017; Barger & Garrod 2020; Sabatini et al. 2020) utilizing both molecular emission and absorption lines.

Simple ions, such as H_3^+, OH^+, and H_2O^+, can be used as a sensitive probe of the cosmic-ray ionization rate. However, these species are typically observed in absorption, and thus most often utilized in regions of diffuse gas. The most straightforward calibration uses the balance of H_3^+ formation and electron

recombination

$$\zeta_{H_2} n(H_2) \approx k_e n(e^-) n(H_3^+)\,, \tag{8.3}$$

resulting in

$$\zeta_{H_2} \approx k_e x_e n_H \frac{n(H_3^+)}{n(H_2)}\,, \tag{8.4}$$

where k_e is the recombination rate, $n(e^-) = x_e n_H$ is the electron abundance, x_e is the electron fraction and $n_H = n(H) + 2n(H_2)$ is the total hydrogen nuclei density (Indriolo & McCall 2012). Measuring local abundances, though, is not possible with absorption measurements, and thus it is often assumed that $n(i) = N(i)/L$, where $N(i)$ is the column density of species i and L is some path length that depends on the geometry of the modeled/observed object. This calibration still relies on constraining the electron fraction, although this can be achieved through measurements of ions such as C^+. However, it can be made more accurate by including information on both the atomic oxygen and carbon monoxide column densities (see e.g., Indriolo & McCall 2012). A similar analysis can be done for utilizing OH^+ and H_2O^+, where the ratio of $N(OH^+)$ and $N(H_2O^+)$ provides the molecular gas fraction and the ratio of $N(OH^+)$ and $N(H)$ provides, in this case, the cosmic-ray ionization rate of atomic hydrogen ζ_H (Indriolo et al. 2015). There have been calibrations developed using both OH and OH^+, namely

$$\zeta_H = 0.67 k_{UV} \frac{n(OH)}{n(H)} \tag{8.5}$$

and

$$\zeta_H = 0.67 \frac{n(OH^+) n(e^-) k_e}{n(H)}\,, \tag{8.6}$$

where k_{UV} is the dissociation rate of OH and k_e is the electron dissociation rate (Indriolo et al. 2015). Again, practically these assume co-spatiality of the different species to convert the abundances to column densities.

Other calibrations have been developed using molecular emission lines with a combination of ions and neutrals, such as N_2H^+, HCO^+, DCO^+, C^+, C, and CO. The simplest of these is the abundance ratio $[HCO^+]/[N_2H^+]$. Both species are formed similarly through H_3^+, although the interaction N_2H^+ with CO further leads to the formation of HCO^+. The presence of free electrons, produced in particular through cosmic-ray ionization processes, decreases this ratio. In regions with strong ζ_{H_2}, N_2H^+ can also be enhanced due to the reduced amount of CO. Using the deuteration chemistry, it is also possible to constrain both the ionization fraction and ζ_{H_2}. Using $R_D \equiv [DCO^+]/[HCO^+]$ and $R_H \equiv [HCO^+]/[CO]$, Caselli et al. (1998) derived two analytic expressions for the ionization fraction

$$x_e = \frac{2.7 \times 10^{-8}}{R_D} - \frac{1.2 \times 10^{-6}}{f_D} \tag{8.7}$$

and for the ionization rate

$$\zeta_{\mathrm{H_2}} = \left[7.5 \times 10^{-4} x_{\mathrm{e}} + \frac{4.6 \times 10^{-10}}{f_{\mathrm{D}}}\right] x_e n(\mathrm{H_2}) R_{\mathrm{H}}\,, \tag{8.8}$$

where f_{D} is a free parameter denoting the amount of depletion of atomic C and O. Analysis using a modified version of the public photo-dissociation region code, 3D-PDR (Gaches et al. 2019), which implemented a spectrum-resolved treatment of cosmic-ray attenuation, has shown that simple analytic calibrations can underestimate $\zeta_{\mathrm{H_2}}$ due to complex ionization gradients. As such, much care needs to be taken to ensure that the emission is co-spatial.

An updated version of Eq. (8.4) has been recently provided by Bovino et al. (2020) for the densest regions of the interstellar medium. The formulation is based on the fact that $\mathrm{H_3^+}$ is converted to its deuterated isotopologues (e.g., $\mathrm{H_2D^+}$) when CO starts to freeze-out ($n_{\mathrm{g}} > 10^4$ cm^{-3}). The final formula reads as

$$\zeta_{\mathrm{H_2}} L = k_{\mathrm{CO}} x_{\mathrm{CO}} \frac{N(\mathrm{H_2D^+})}{3R_{\mathrm{D}}}\,, \tag{8.9}$$

where k_{CO} is the rate of the proton-transfer reaction between $\mathrm{H_3^+}$ and CO, and $x_{\mathrm{CO}} = n(\mathrm{CO})/n_{\mathrm{H}}$ the CO abundance. The above formula has been validated via 3D magneto-hydrodynamic simulations providing a correction factor α (Bovino et al. 2020), and applied to observations of high mass clumps by Sabatini et al. (2020).

Besides analytic expressions, the cosmic-ray ionization rate can be constrained using multiple emission and/or absorption lines and astrochemical models. With these models, there is a sacrifice of ease-of-use and necessity to run numerous astrochemical models, but with the advantage of more accurate chemistry (see e.g., Caselli et al. 1998; van der Tak & van Dishoeck 2000; McCall et al. 2002, 2003; Hezareh et al. 2008; Shaw et al. 2008; Ceccarelli et al. 2011; Hollenbach et al. 2012; Indriolo & McCall 2012; Ceccarelli et al. 2014; Podio et al. 2014; Vaupré et al. 2014; Cleeves et al. 2015; Indriolo et al. 2015; Le Petit et al. 2016; Fontani et al. 2017; Neufeld & Wolfire 2017; Favre et al. 2018; Indriolo et al. 2018; Bacalla et al. 2019; Barger & Garrod 2020; Redaelli et al. 2021). These methods can range from grids of 0D models, in which the density is held constant, to post-processing time-dependent three-dimensional simulations. However, we urge caution when constraining $\zeta_{\mathrm{H_2}}$ from molecular line ratios: much care needs to be taken to constrain the gas temperatures being traced, the co-spatiality of the tracers, and time-dependent effects. Further, the decision of whether to include cosmic-ray attenuation can influence the end results.

Recently, it has been proposed to use ro-vibrational lines from $\mathrm{H_2}$ as a direct probe for the cosmic-ray ionization rate (Bialy 2020). Here, $\mathrm{H_2}$ is excited to higher ro-vibrational levels through excitation by secondary electrons produced through cosmic-ray interactions with $\mathrm{H_2}$. Since the distribution of secondary electrons is dependent on the spectrum of primary cosmic rays (Dalgarno et al. 1999; Ivlev et al. 2021), this method may be a unique method to constrain the

cosmic-ray spectrum and the ionization rate in molecular gas, independent of the chemistry (Bialy 2020; Bialy et al. 2022; Padovani et al. 2022). Many such diagnostics may be found as more astrochemical computations include spectrum-dependent cosmic-ray physics.

The ionization rates estimated by the various observational methods above show a wide spread of values. As shown in the top panel of Fig. 8.4, the $\zeta_{\rm H}$ values in diffuse clouds far from the Galactic center, on average between 10^{-17} and 10^{-15} s^{-1}, are independent of the column density of atomic hydrogen. Conversely, close to the Galactic center $\zeta_{\rm H}$ increases by about one order of magnitude, likely because these clouds are close to cosmic-ray sources. Estimates of the ionization rate at higher and higher column densities, where hydrogen is in molecular form, so in this case, one gets $\zeta_{\rm H_2}$, show instead a decrease as the H_2 column density increases. As shown in the bottom panel of Fig. 8.4, excluding active regions such as supernova remnants or massive hot cores, the decrease of $\zeta_{\rm H_2}$ at high column densities can be appreciated. This panel also shows some trends of $\zeta_{\rm H_2}$ predicted in the continuous-slowing down approximation (Sect. 8.3.2.1) for different values of the low-energy slope α (Sect. 7.5) for comparison. We note that, assuming diffusive propagation of cosmic rays (Sect. 8.3.2.2), the case $\alpha = -1.2$ better reproduces the average value of the cosmic-ray ionization rate in diffuse clouds (Silsbee & Ivlev 2019).

SUGGESTION 8.2

Since the ionization rate turns out to be a function of the H_2 column density in the densest parts of a molecular cloud Sect. 8.3.2, it is useful to incorporate into astrochemical codes the $\zeta_{\rm H_2}(N)$ prescriptions provided, for example, by Padovani et al. (2018b) and Silsbee & Ivlev (2019) for the free streaming and diffusive regimes, respectively.

8.1.2 On the role of magnetic fields

It is important to remember that ionization rate estimates derived from observations are based on molecular abundances measured along the line of sights. In Fig. 8.4, the column density of H_2 on the x-axis is also measured along the line of sights. However, cosmic rays are charged particles, and, as they propagate, they move along magnetic field lines following a spiral motion. This means that the line-of-sight column density can be smaller than that passed through by cosmic rays (sometimes called *effective column density*).

Observations of polarized dust emission show that the magnetic field topology is uniform in the most diffuse regions, tending then to concentrate in the denser regions (assuming the so-called hourglass shape), until it becomes increasingly toroidal in the denser regions where the protostar formation will occur (Hennebelle & Ciardi 2009; Joos et al. 2012; Padovani et al. 2013). It can then be assumed that line-of-sight and effective column densities coincide in diffuse re-

gions, but this approximation becomes less and less accurate as one approaches the central protostar. This should be considered whenever observational estimates are compared with those derived from theoretical models.

8.2 COSMIC RAYS INDUCED ULTRAVIOLET RADIATION

When an H_2 molecule becomes collisionally-excited into higher electronic states, the molecular can radiative decay back to the ground state and emit ultraviolet radiation (Cravens & Dalgarno 1978). In dense gas, shielded by ultraviolet radiation, electrons, mainly secondary electrons, will collisionally excite H_2, producing a source of ultraviolet radiation in dense, shielded gas. This mechanism, often called the Prasad-Tarafdar mechanism, following the seminal work in Prasad & Tarafdar (1983), can become an important source of photodissociation in molecular clouds (see e.g. Gredel et al. 1989).

Following Heays et al. (2017), we denote the photo-destruction rate of some species, X, due to cosmic-ray induced UV photons, often called *cosmic-ray photons*, as

$$k_{\rm X} = \frac{1}{x_{\rm X}} \int R(\lambda) p_{\rm X}(\lambda) {\rm d}\lambda, \tag{8.10}$$

where $x_{\rm X} = n({\rm X})/[n({\rm H}) + 2n({\rm H_2})]$, $R(\lambda)$ is the rate of photon production following cosmic-ray ionization and $p_{\rm X}$ is the fraction of photons that lead to the photodestruction or ionization of species X. The rate of photon production, $R(\lambda)$ is related directly to the cosmic-ray ionization rate

$$R(\lambda) = \zeta_{\rm H_2} x({\rm H_2}) P(\lambda), \tag{8.11}$$

where $P(\lambda)$ is the wavelength probability distribution of the induced photons (Gredel et al. 1989). For diffuse clouds, or regions with substantial atomic hydrogen, the cosmic-ray ionization of hydrogen can be directly added to the above relation.

When an H_2 molecule emits an ultraviolet photon, there is a significant chance that the photon is absorbed by dust grains. The photon can further be absorbed by other molecular and atomic species. Therefore, the fraction of ultraviolet photons which lead to the photodissociation or ionization of species, X, can be written

$$p({\rm X}) = \frac{x_{\rm X} \sigma_{\rm X,diss,ion}}{x_{\rm dust}\sigma_{\rm dust} + \sum_k x_{\rm X_k} \sigma_{\rm X_k,diss,ion}}, \tag{8.12}$$

where the denominator includes both photoabsorption of dust ($\sigma_{\rm dust}$) and other species $\rm X_k$. Under the assumption that only dust absorption is significant, the expression for $p({\rm X})$ reduces to that from Gredel et al. (1989); McElroy et al. (2013).

Cosmic-ray-induced photodissociation and ionization can be included in astrochemical networks with a term similar to that of cosmic-ray ionization,

$$R_{\rm diss,ion} = n({\rm X}) k_X = n({\rm X}) \left(\frac{\zeta_{\rm H_2}}{10^{-16}\ {\rm s^{-1}}} \right) k_{\rm X,0}, \tag{8.13}$$

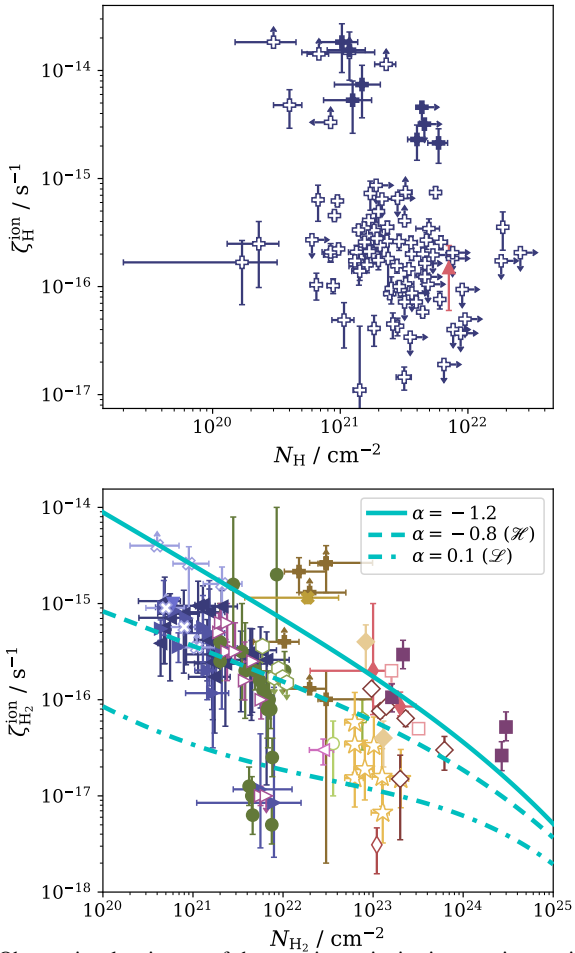

FIGURE 8.4 Observational estimates of the cosmic-ray ionization rate in atomic and molecular regions (upper and lower panel, respectively). Data for $\zeta_{\rm H}$ in diffuse regions (solid up-pointing triangle, Neufeld et al. 2010), in the Galactic disk and in the Galactic center (empty and solid plus signs, respectively, Indriolo et al. 2015). Data for $\zeta_{\rm H_2}$ in diffuse regions (solid down-pointing triangle, Shaw et al. 2008; solid left-pointing triangles, Indriolo & McCall 2012; solid right-pointing triangles, Neufeld & Wolfire 2017; empty right-pointing triangles, Luo et al. 2022), in low-mass dense cores (solid circles, Caselli et al. 1998; empty circle, Maret & Bergin 2007; empty pentagon, Fuente et al. 2016; empty left-pointing triangle, Redaelli et al. 2021; empty hexagons, Bialy et al. 2022), in high-mass star-forming regions (empty stars, Sabatini et al. 2020; solid diamonds, de Boisanger et al. 1996; empty diamonds, van der Tak & van Dishoeck 2000; empty thin diamond, Hezareh et al. 2008; solid thin diamonds, Morales Ortiz et al. 2014), in circumstellar discs (empty squares, Ceccarelli et al. 2004), in massive hot cores (solid squares, Barger & Garrod 2020), and in supernova remnants (empty crosses, Indriolo et al. 2010; solid cross, Ceccarelli et al. 2011; solid plus signs, Vaupré et al. 2014). The cyan lines in the lower panel show models of $\zeta_{\rm H_2}$ as a function of the H_2 column density for three values of the low-energy slope of the cosmic-ray flux (see Sect. 7.5).

where $k_{X,0}$ are the rates calculated by Heays et al. (2017). Tab. 8.2 shows the cosmic-ray photon reaction rates from Heays et al. (2017), where they calculated the rates assuming an H_2 cosmic-ray ionization rate, $\zeta_{H_2} = 10^{-16}$ s^{-1}, a Doppler broadening parameter, $b = 1$ km s^{-1} and H_2 entirely in the para-form. The wavelength probability distribution, $P(\lambda)$, was derived with significant assumptions on the spectrum of secondary electrons (Gredel et al. 1989).

SUGGESTION 8.3

The ideal way to compare observations and models, especially in regions where the geometry of the magnetic field is far from uniform, would be to use numerical simulations generated from chemical-dynamic codes that also include the evolution of the magnetic field. In this way, it would be possible to compare observed and synthetic abundances of molecular species much more accurately, to estimate the ionization rate based on the effective column density traversed by cosmic rays.

8.3 COSMIC-RAY PHYSICS

8.3.1 Cosmic-ray transport primer

Cosmic-ray transport is a complicated subject due to the non-linear coupling between cosmic rays and magnetic fields. Due to their charged nature, the trajectory of cosmic rays is coupled to the morphology and evolution of magnetic fields, while cosmic rays induce changes in the local magnetic field through their current. As such, theoretical investigations of cosmic-ray physics often rely on one of two assumptions:

- **test wave** approximation: the distribution of cosmic rays is held constant while their impact on the magnetic fields is computed;
- **test particle** approximation: the magnetic fields are fixed, and the resulting cosmic-ray distribution is computed.

There have been many monographs and reviews about the transport of cosmic rays in different environments. Here, we will focus on transport through molecular gas.

The motion of cosmic rays is tightly coupled to the electromagnetic field according to the Lorentz force

$$\frac{\mathrm{d}\mathbf{p}}{\mathrm{d}t} = q\left(\mathbf{E} + \frac{\mathbf{v}}{c} \times \mathbf{B}\right) , \tag{8.14}$$

where $\mathbf{p} = \gamma m \mathbf{v}$ is the momentum, $\gamma = 1/\sqrt{1 - \mathbf{v}^2/c^2}$ is the Lorentz factor, and q is the particle charge. Large-scale electric fields increase the energy of the cosmic ray, while magnetic fields induce a spiral motion. The scale of the spiral motion is characterized by the particle gyroradius

$$r_g = \frac{pc}{qB} \sin\alpha , \tag{8.15}$$

where α is the pitch angle, the angle between the particle's velocity and the magnetic field. For particles of interest to astrochemistry, the gyroradius is much smaller than the physical scales of interest. Due to turbulence, cosmic rays can scatter, through both resonant and non-resonant processes, across magnetic field lines. The transport of cosmic rays is often treated as a diffusion-loss equation. With $n_i(E)$ representing the number of cosmic rays of species i per unit volume and energy, the resulting diffusion-loss equation can be written as (Longair 2011)

$$\frac{\partial n_i}{\partial t} = \underbrace{D(E)\nabla^2 n_i}_{\text{Diffusion}} + \underbrace{\frac{\partial}{\partial E}\left[b(E)n_i\right]}_{\text{Continuous Losses}} + \underbrace{\frac{1}{2}\frac{\partial^2}{\partial E^2}\left[d(E)n_i(E)\right]}_{\text{Acceleration}} - \underbrace{\frac{n_i}{\tau}}_{\text{Catastrophic Losses}} + \underbrace{Q_i}_{\text{Sources}} . \tag{8.16}$$

The terms on the right-hand side are annotated with their physical basis. The first term denotes spatial diffusion, here assuming isotropic diffusion with diffusion coefficient, D. The second term describes continuous losses: interactions leading to a loss of particle energy in which the energy loss is small with respect to the current particle energy, described by an energy-loss rate, $b(E) = \mathrm{d}E/\mathrm{d}t$. This term is related to the loss function, $L_i(E)$ by $b(E) = -n_g v_i(E) L_i(E)$, where n_g is the hydrogen-nuclei number density of the gas and $v_i(E)$ is the velocity of the cosmic-ray species, i. The loss function, and how to calculate it, is described in Sect. 8.4. The third term corresponds to diffusion in energy space, leading to (de)acceleration, with coefficient $d(E)$. We will discuss later in the section what leads to (de)acceleration of cosmic rays. The fourth term describes catastrophic losses, in which the particle loses enough energy to return it to the thermal distribution on timescales τ. Finally, the latter term describes local sources of cosmic rays, where the acceleration of sources (which can act as a source term) is described in Sect. 8.3.3. These terms will be discussed below concerning different regimes of cosmic-ray transport and the acceleration of cosmic rays from thermal distributions. While the equation of transport, Eq. (8.16) is written in terms of the differential number density of cosmic rays, it is often convenient to express it in terms of a flux of cosmic rays, j_i, in units particles cm^{-2} s^{-1} sr^{-1}. These two are related by

$$j(E) = \frac{v_i(E) n_i(E)}{4\pi}, \tag{8.17}$$

where $v_i(E)$ is the velocity of cosmic-ray species, i, at energy, E. In general, solving Eq. (8.16) in its complete form is numerical complex, although some codes such as Galprop (Moskalenko & Mashnik 2003) and Dragon2 (De La Torre Luque et al. 2021) do so. Here, we will discuss approximations of

this equation that are most relevant for molecular clouds and provide analytic or semi-analytic functions which can be most readily implemented in astrochemical models.

8.3.2 Different Regimes of Transport

As described above, the dynamics of cosmic rays is strongly coupled to the magnetic fields. For low-energy cosmic rays, which regulate the thermochemistry of molecular clouds, their gyroradii are small compared to the sizes of molecular clouds. However, turbulence induces diffusion of the magnetic field lines, and thus cosmic rays can scatter across field lines and diffuse through the gas. Here, we describe two different limiting cases of cosmic-ray transport:

- **free-streaming**, in which cosmic rays stream out along magnetic field lines without a significant number of scattering events;
- **diffusive**, in which there are sufficient scattering events to induce a diffusion-like transport of cosmic rays.

In the following, we focus solely on the transport of CRs into molecular gas from external sources. Transport from point sources, and other embedded sources, is little constrained in cloud environments (although see e.g., Fitz Axen et al. 2021) while some studies have investigated the transport from T-Tauri stars through protoplanetary disks (Rab et al. 2017; Rodgers-Lee et al. 2017; Fraschetti et al. 2018).

8.3.2.1 Free-Streaming Transport

The free-streaming approximation, also called the continuously slowing-down approximation (CSDA) (Takayanagi 1973), is the limiting regime where scattering is inefficient, thereby inhibiting diffusion so that cosmic rays merely stream along the magnetic field lines. Under this approximation, the flux of cosmic rays (also known as *spectrum*), namely the number of cosmic rays per unit energy, time, area, and solid angle, j, at effective column density[2], N, is related to the surface flux by

$$j(E, N, \mu)L(E) = j_{\rm IS}(E_i, \mu)L(E_i)\,, \tag{8.18}$$

where E and E_i is the current and initial energy, respectively, $L(E)$ is the loss function at energy E, $j_{\rm IS}$ is the interstellar flux irradiating the surface of a molecular cloud, and μ is the cosine of the pitch angle. The loss function describes the quantity of energy lost by a cosmic ray after passing through a column density N and is related to the energy loss per unit of time, $\mathrm{d}E/\mathrm{d}t$, by

$$L(E) = -\frac{\mathrm{d}E}{\mathrm{d}N} = -\frac{1}{n_{\rm g} v(E)}\frac{\mathrm{d}E}{\mathrm{d}t} = -\frac{1}{n_{\rm g} v(E)} b(E)\,, \tag{8.19}$$

2. The effective column density is the column density of gas traversed by a cosmic-ray particle before it reaches a given point.

where n_g is the volume density of the medium and v is the cosmic-ray velocity (see Sect. 8.4 for the derivation of the loss function). The energy, E, is the energy of the cosmic ray after propagating through an effective column density, N, while undergoing losses from the initial energy, E_i. As such, they are related through

$$N = \mu \int_E^{E_i} \frac{\mathrm{d}E}{L(E)} \,. \tag{8.20}$$

Similarly, the particle's range, $R(E)$, which describes the *path length* necessary to return the particle to the thermal tail, follows from the loss function,

$$R(E) = \frac{1}{n} \int_0^{E} \frac{\mathrm{d}E}{L(E)} \,. \tag{8.21}$$

Using this, we can rewrite Eq. (8.20) as

$$N = \mu n \left[R(E) - R(E_0) \right] \,. \tag{8.22}$$

SUGGESTION 8.4

The energy of a particle with initial energy, E_0, after propagating through an effective column density, N, can be found by numerical inversion. In particular, by introducing the stopping column,

$$\mathcal{N}(E) \equiv nR(E) = \int_0^{E} \frac{\mathrm{d}E}{L(E)} \,, \tag{8.23}$$

we can rewrite Eqs. (8.20-8.22) as

$$\mathcal{N}(E) = \frac{N}{\mu} + \mathcal{N}(E_0) \,. \tag{8.24}$$

Numerically inverting this function can typically be performed more rapidly from precomputed loss functions versus solving for contours in $E - E_0$ space using Eq. (8.22).

We can make a few simple approximations to understand how, under the CSDA, the flux varies with column density. Consider an initial power-law proton flux,

$$j(E) = j_0 \left(\frac{E}{E_0} \right)^{-a} \,. \tag{8.25}$$

For the energies which dominate the chemistry, the loss function has been found to be reasonably reproduced by a power-law (Padovani et al. 2018b; Silsbee & Ivlev 2019)

$$L(E) = L_0 \left(\frac{E}{E_0} \right)^{-b} \,, \tag{8.26}$$

where $L_0 = 1.27 \times 10^{-15}$ eV cm^2, $E_0 = 10^6$ eV, and $b = 0.82$. From the prescribed loss function, we get the stopping column

$$\mathcal{N}(E) = \frac{E_0}{(1+b)L_0}\left(\frac{E}{E_0}\right)^{1+b} . \tag{8.27}$$

Combining the above relations, the flux at effective column density, N, is

$$\boxed{j(E, N, \mu) = j_{\rm IS}(E)\left[1 + \frac{N}{\mu\mathcal{N}(E)}\right]^{-\frac{a+b}{1+b}} .} \tag{8.28}$$

From this relation, we can immediately see that for particles whose range is significantly greater than the column density, $(E) \gg N$, the flux is unchanged from the interstellar one. We can also see that the flux is explicitly dependent solely on the effective column density through which the cosmic ray has traveled and not on any other properties of the molecular gas, such as the degree of turbulence, strength and morphology of the magnetic fields, etc. However, these later properties can be hidden in the effective column density: e.g., if the magnetic field lines are tangled, the effective column density will be significantly greater than the line-of-sight column density.

8.3.2.2 Diffusive Transport

Recalling the CR transport equation, Eq. (8.16), the diffusion-loss equation can be written

$$\frac{\partial n_i}{\partial t} = D(E)\nabla^2 n_i + \frac{\partial}{\partial E}\left[b(E)n_i\right] , \tag{8.29}$$

where $D(E)$ is the isotropic diffusion coefficient. There are two primary avenues of diffusion: extrinsic and intrinsic scattering. Extrinsic scattering by resonant scattering of cosmic rays by magneto-hydrodynamic waves occurring in the turbulent cascade. Intrinsic scattering can occur through waves self-generated by cosmic rays, leading to streaming instabilities. For the discussion in this chapter, we focus on extrinsic scattering sources, in particular, scattering via magneto-hydrodynamic turbulence. Recently, it has been proposed that cosmic rays can non-resonantly scatter through the superdiffusion of magnetic field lines (Lazarian & Yan 2014; Lazarian & Xu 2021).

The assumption of an isotropic diffusion coefficient only holds for weak magneto-hydrodynamic turbulence. Under strong turbulence, the magnetic field turbulence is transported differently parallel and perpendicular to the mean magnetic field direction. Therefore, there is both a parallel and perpendicular diffusion coefficient, $D_\parallel$ and $D_\perp$, respectively. For simplicity, we focus on weak turbulence to allow for an isotropic treatment of diffusion. The value of the diffusion coefficient in molecular gas is poorly constrained in molecular clouds, with values ranging from $D \approx 10^{27} - 10^{30}$ cm^2 s^{-1} (e.g., Gabici 2011; Dogiel et al. 2015; Evoli et al. 2020; Owen et al. 2021). For more in-depth discussions regarding the

diffusion of cosmic rays, the reader is referred to Yan & Lazarian (2004); Strong et al. (2007); Zweibel (2013); Schlickeiser (2015); Amato & Blasi (2018).
Under these assumptions, we follow Skilling (1975) to parameterize the diffusion coefficient as

$$D(E) = \frac{vB^2}{6\pi^2 \mu k_{\rm res}^2 W(k_{\rm res})}\,, \tag{8.30}$$

where v is the cosmic-ray velocity, B is the average magnetic field, $W(k_{\rm res})$ is the turbulence power spectrum and $k_{\rm res}$ is the resonant scattering wavelength. The resonant scattering follows the relation

$$k_{\rm res}(E) = \frac{m\Omega}{\mu p(E)}\,, \tag{8.31}$$

where m is the cosmic-ray particle mass, $\Omega = eB/mc$ is the gyrofrequency, and e is the elementary charge. Therefore, to proceed, one must prescribe a turbulence model. Here, we assume

$$kW(k) \approx \frac{1}{2}\rho_{\rm ion}\sigma_{\rm turb}^2\,, \tag{8.32}$$

where $\rho_{\rm ion}$ is the ion mass density and $\sigma_{\rm turb}$ can be described by a linewidth-size relation, $\sigma_{\rm turb}(k) \propto k^{-\lambda} \propto \ell^{\lambda}$ for length scale $\ell = 1/k$ and assuming a model of turbulence which sets λ. Assuming the ion density is constant, the diffusion coefficient is

$$D(E) \propto E^{1-\lambda}\rho_{\rm ion}^{-1}\,. \tag{8.33}$$

Silsbee & Ivlev (2019) showed that these relations lead to

$$\boxed{j(E,N) = j_{\rm IS}(E)\int_0^1 \operatorname{erfc}\left[\frac{N/N_0}{\sqrt{(E/E_0)^{\alpha}\left(x^{-\frac{-\alpha}{\alpha+b}}-1\right)}}\right]{\rm d}x\,,} \tag{8.34}$$

where $\alpha = \frac{3}{2} + b - \lambda$,

$$N_0 = \sqrt{\frac{4nD_0E_0}{\alpha v_0 L_0}}\,, \tag{8.35}$$

is the characteristic attenuation column density, $v_0^2 = 2E_0/m$ and $D_0 = D(E_0)$. To determine a solution, a model for the turbulence must be chosen that determines λ, where, for instance, $\lambda = 1/3$ and $\lambda = 1/4$ correspond to Kolmogorov and Kraichnan turbulence, respectively.
Diffusive transport is a naturally complicated problem due to the stronger coupling of the cosmic-ray transport to the strength and physics of magneto-hydrodynamic turbulence, instabilities, and magnetic morphologies. Therefore, numerical solutions of the transport equation may be necessary to determine the cosmic-ray flux throughout molecular gas.

8.3.2.3 Cosmic-ray propagation at very high column densities

In this section, we give an overview of the challenges in modeling cosmic-ray propagation at column densities typical of circumstellar disks. For a complete treatment of the problem, we refer to Umebayashi & Nakano (1981) and Padovani et al. (2018b).

In general, the propagation of primary and secondary (Sect. 8.3.4) cosmic rays shall be computed in the CSDA, the diffusion approximation, or the catastrophic approximation by adopting a matching procedure depending on the different transport regimes. The latter depends on the nature of the dominant loss process, modeled as continuous or catastrophic (Sect. 8.4). At moderate-to-high column densities ($N_{H_2} \gtrsim 10^{25}$ cm^{-2}), the CSDA no longer applies.

Cosmic-ray protons with energy larger than 280 MeV interact with H_2 leading to pion production. Since the pion rest mass is non-negligible[3], protons lose a significant energy fraction during the collision, so there is a transition between the CSDA regime, which works for energies lower than about 25 MeV and the diffusive regime, above about 1 GeV.

Neutral pions, whose lifetime is 8.5×10^{-17} s, decay into photon pairs ($\pi^0 \rightarrow 2\gamma$) and charged pions, whose lifetime is 2.6×10^{-8} s, become electrons and positrons through muon decay ($\pi^{\pm} \rightarrow \mu^{\pm} \rightarrow e^{\pm}$). Finally, another source of photons is bremsstrahlung by electrons and, in turn, photons decay in electron-positron pairs ($\gamma \rightarrow e^{\pm}$).

The regime of photon propagation depends on their energy: photoionization and pair production dominate below about 5 keV and above about 50 MeV. These processes are both catastrophic. At intermediate energies, where Compton scattering dominates, there is a transition to the diffusive regime.

Finally, for electrons with energies larger than about 500 MeV, bremsstrahlung overcomes ionization losses. The energy of the photon created by bremsstrahlung is of the same order as that of the electron that generated it (Ginzburg & Syrovatskii 1964). This means that bremsstrahlung can approximately be treated as a catastrophic process.

The study of cosmic-ray propagation at typical densities of circumstellar disks should carefully take into account the various propagation regimes, since ionization due to secondary particles, in particular electron-positron pairs, is responsible for the ionization of the medium at column densities larger than about 8×10^{25} cm^{-2}.

8.3.3 Acceleration of Cosmic Rays

The acceleration of charged particles to relativistic energies has been long-considered and debated (see reviews by Melrose 2009; Schure et al. 2012; Bell 2013; Blasi 2013; Blandford et al. 2014). The general problem of CR acceleration

3. The mass of neutral pions (π^0) is 135.0 MeV c^{-2} and that of charged pions ($\pi^{\pm}$) is 139.6 MeV c^{-2}.

is to explain how particles are accelerated from a thermal Maxwellian to a nonthermal power-law distribution, with the measured CR spectrum extending to over 10^{20} eV. There have been several potential acceleration mechanisms proposed over the decades, with stochastic acceleration (so-called second-order Fermi acceleration, Fermi 1949, 1954) and shock acceleration being the most historically significant.

Here we highlight the process of diffusive shock acceleration, also known as first-order Fermi acceleration, introduced over a series of papers in the late 1970s to early 1980s (Axford et al. 1977; Krymskii 1977; Bell 1978a,b; Blandford & Ostriker 1978; Drury 1983). Diffusive shock acceleration is thought to be the dominant process in the acceleration of cosmic rays by supernovae, the most probable, and dominant, sources of Galactic cosmic rays. Here, we will follow the simpler, but more intuitive, microphysical derivation following Bell (1978a). While this method assumes relativistic particles and parallel magneto-hydrodynamic shocks, the end results are close to more sophisticated, but less physically intuitive, approaches.

Let us envisage a shock, propagating at speed u_s. In the rest frame of the shock, we denote the velocity of scatters upstream and downstream from the shock by u_1 and u_2, respectively. These are related by

$$\frac{u_1}{u_2} = \frac{(\gamma_g + 1)\mathcal{M}_s^2}{(\gamma_g - 1)\mathcal{M}_s^2 + 2}\,, \tag{8.36}$$

where γ_g is the gas adiabatic index, $\mathcal{M}_s = u_s/c_s$ is the sonic Mach number of the shock and c_s is the sound speed in the downstream region. This ratio is also defined as the shock compression factor, $r = u_1/u_2$. For a non-relativistic shock, $r \to 4$ in the high Mach number limit.

The shock is assumed to be super-Alfvénic, enabling energetic particles to generate turbulence in the form of self-generated Alfvén waves. As the particles scatter, the streaming velocity of the escaping particles is reduced to the Alfvén speed through wave dampening, ensuring the shock overtakes them once again. Therefore, the particles scatter between the downstream and upstream regions, gaining energy through each shock crossing. As such, the method of scattering is self-provided: the energetic particles generate the Alfvén waves, producing the turbulence which allows them to diffusely scatter. To derive the resulting particle spectrum, in steady-state, we consider the balance of the number of particles escaping downstream the shock and the energy gain of the particles after each shock crossing.

The net flux of particles advected away in the downstream region is simply $N_{CR}u_2$, where N_{CR} is the number of energetic particles. The number of particles crossing from the upstream to the downstream region is, nominally, $N_{CR}c/4$, where the factor of 4 comes by assuming an isotropic distribution and averaging over the angle of crossing. The fraction of particles escaping downstream is thus $N_{CR}u_2/(N_{CR}c/4) = 4u_2/c$. Thus, the probability of a particle crossing

the shock and not being advected away is $P = \left(1 - \frac{4u_2}{c}\right)$, and after m crossing, $P_m = \left(1 - \frac{4u_2}{c}\right)^m$. If we assume a strong non-relativistic shock, this reduces simply to $P_m = \left(1 - \frac{u_s}{c}\right)^m$. Therefore, the number of particles surviving m crossings is related to the initial number $N_{0,\mathrm{CR}}$,

$$\frac{N_{\mathrm{m,CR}}}{N_0} = \left(1 - \frac{u_s}{c}\right)^m . \tag{8.37}$$

After a particle crosses the shock interface, from performing the appropriate Lorentz transformation and averaging over angles, we find that the average energy gain is

$$\frac{\Delta E}{E} \approx \frac{u_s}{c} . \tag{8.38}$$

Similar to the above analysis, the energy gain of the particle after m crossings is thus

$$\frac{E_m}{E_0} = \left(1 + \frac{u_s}{c}\right)^m . \tag{8.39}$$

Assuming $u_s \ll c$, we can rewrite $\left(1 + \frac{u_s}{c}\right)^m \approx \left(1 - \frac{u_s}{c}\right)^{-m}$. Comparing these expressions, we find that

$$\frac{N_m}{N_0} \approx \left(\frac{E_m}{E_0}\right)^{-1} . \tag{8.40}$$

This gives the familiar result for the differential energy spectrum

$$n_{\mathrm{CR}}(E) = \mathrm{d}N(E)/\mathrm{d}E \propto E^{-2} . \tag{8.41}$$

A more thorough analysis of leads to a dependence of the differential energy spectrum on the shock compression factor, r,

$$\boxed{n_{\mathrm{CR}}(E) \propto E^{-q+2}}, \tag{8.42}$$

where $q = \frac{3r}{r-1}$.

The maximum energy possible for the acceleration is generally determined by restrictions due to the energy losses, Alfvén wave dampening, and diffusion away from the shock. However, we can calculate the upper limit on the maximum energy using the argument laid out by Syrovatsky (1970), following Longair (2011). Here, we consider the maximum amount of energy available if all the magnetic field energy is converted over the shock's lifetime into particle acceleration. We can rewrite Faraday's law

$$\nabla \times \mathbf{E} = -\frac{\partial \mathbf{B}}{\partial t} , \tag{8.43}$$

using an order of magnitude approximation, assuming that the shock acceleration happens in some length scale, L, over some timescale, L/u_s,

$$\frac{|\mathbf{E}|}{L} \approx \frac{|\mathbf{B}|}{L/u_s} . \tag{8.44}$$

The particles gain energy as from this induced electric field, and over the length scale of the acceleration region, this leads to

$$E_{\rm CR,max} \approx Ze|\mathbf{B}|u_{\rm s}L\,, \tag{8.45}$$

for a particle with total charge, Ze.

In recent years, there has been increasing interest in the search for local cosmic-ray sources other than supernova remnants. For this, we suggest a series of papers on the local acceleration of cosmic rays in protostellar shocks (Padovani et al. 2015, 2016; Rodgers-Lee et al. 2017, 2020; Fitz Axen et al. 2021; Padovani et al. 2021b), in protostellar clusters (Gaches & Offner 2018; Gaches et al. 2019), and in expanding HII regions (Padovani et al. 2019).

8.3.4 Secondary Electron Production

When cosmic rays interact with gas, they can knock electrons out of their potentials with some excess energy. There have been several studies describing the production of secondary electrons from interactions of cosmic rays and neutral gas (Knipp et al. 1953; Erskine 1954; Spencer & Fano 1954; Dalgarno & Griffing 1958; Cravens & Dalgarno 1978; Xu & McCray 1991; Gredel & Dalgarno 1995; Dalgarno et al. 1999; Ivlev et al. 2021). These induced generations of electrons can themselves produce more ionizations, thus leading to a cascade. We adopt the nomenclature that all induced electrons are considered *secondary*, to differentiate against *primary* electrons, which constitute the interstellar contribution. Here, we will show the derivation of the secondary electron flux for ionizing electrons, loosely following Ivlev et al. (2015).

The column density, $\mathcal{N}_{\rm stop}$, required to return a non-thermal electron to the electron bath, from Eq. (8.23), is

$$\mathcal{N}_{\rm stop}(E) = \int_0^E \frac{{\rm d}E'}{L_e(E')}, \tag{8.46}$$

where $L_e(E)$ is the electron loss function. For the low-energy electrons expected from secondary processes, namely $E < 1$ keV, the stopping column is $\mathcal{N}_{\rm stop} < 10^{18}$ cm^{-2}. Therefore, given the column density of molecular clouds, $N > 10^{22}$ cm^{-2}, it is valid to consider the production of secondary electrons as a *local* process, without regarding their transport. Using this local approximation, their stopping time is

$$t_{\rm stop}(E) = \frac{E}{n_g v_e L_e(E)}\,, \tag{8.47}$$

where n_g is the gas particle number density and v_e is the electron velocity.

The source term for the production of secondary electrons can be described as the product of the probability an electron is produced per interaction and the number density of targets, i.e.

$$\Phi(E_e) = 4\pi n_g \sum_i \int_{I+E}^{\infty} \frac{{\rm d}\sigma(E_i, E_e)}{{\rm d}E_e} j_i(E_i){\rm d}E_i, \tag{8.48}$$

where the summation is carried out over different interacting cosmic-ray species, i, with flux $j_i(E_i)$ and a different production cross section, $\mathrm{d}\sigma(E_i, E_e)/\mathrm{d}E_e$ (e.g., described above), $I = 15.426$ is the H_2 ionization potential and $\Phi(E_i)$ is in units of particles $\mathrm{cm}^{-3}\,\mathrm{eV}^{-1}\,\mathrm{s}^{-1}$. Here, we assume that the production of secondary electrons is roughly isotropic.
We can transform this into a more familiar formulation. First, let us consider the differential number density of secondary electrons,

$$\begin{aligned}\frac{\mathrm{d}N_{\mathrm{sec,e}}}{\mathrm{d}E\,\mathrm{d}V} &= \Phi(E_e)t_{\mathrm{stop}}(E)\\ &= \frac{4\pi E}{v_e L_e(E)}\int_{I+E}^{\infty}\frac{\mathrm{d}\sigma(E_i,E_e)}{\mathrm{d}E_e}j_i(E_i)\mathrm{d}E_i.\end{aligned} \tag{8.49}$$

From this, the flux of secondary electrons follows from $\frac{\mathrm{d}N_{\mathrm{sec,e}}}{\mathrm{d}E\mathrm{d}V} = (4\pi/v_e)j_{\mathrm{sec,e}}$:

$$\boxed{j_{\mathrm{sec,e}} = \frac{E}{L_e(E)}\int_{I+E}^{\infty}\frac{\mathrm{d}\sigma(E_i,E_e)}{\mathrm{d}E_e}j_i(E_i)\mathrm{d}E_i.} \tag{8.50}$$

We note that the flux is not directly dependent on the gas density, but only on the production cross sections and primary cosmic-ray flux. A more rigorous derivation, including both production and depopulation, leads to an integro-differential equation for the spectrum (see e.g., Ivlev et al. 2021). However, for ionizing secondary electrons, using the above more approximate treatment produces minimal errors. At lower energies, the spectrum of secondary electrons depends greatly on the used excitation cross sections, with more recent cross sections substantially changing the non-ionizing secondary electron spectrum. Both the ionization and excitation cross sections will be discussed in the following section.

8.3.5 Common Implementations of Cosmic-ray Chemistry

Cosmic-ray chemical effects and phenomenon such as secondary-electrons and induced FUV emission has been routinely implemented in astrochemical codes to various different degrees of complexity. In nearly all astrochemical codes, the chemical networks include prescriptions for secondary FUV ionization or dissociation (see e.g., the bottom of Tab. 8.2), while secondary electrons are often included by just multiplying the primary ionization rate by some constant factor. Cosmic-ray transport is often neglected, although more recent studies have begun to include transport alongside chemistry using various methods and approximations. In ascending order of complexity, these different implementations are:

- Constant ionization rate (no transport): This is the most common approach in astrochemical codes, where a globally constant ionization rate is chosen, or varied to perform parameter studies.

- Spatial/temporal variation of the ionization rate: In these implementation methods, either the user provides, the program has implemented some function or tabulation of the ionization rate, most commonly as a function of column density, e.g. $\zeta(N)$ (see e.g., Rimmer et al. 2012; Cleeves et al. 2013; Redaelli et al. 2021; Gaches et al. 2022; O'Donoghue et al. 2022), or there is some solution of the total ionization rate (e.g., Grassi et al. 2019; Fujii & Kimura 2022). The most commonly implemented prescribed functions are the high- and low-models from Padovani et al. (2018c). An example of a public code that has implemented this is UCLCHEM[4] (O'Donoghue et al. 2022)
- One-dimensional solutions: There have been several studies that have coupled a numerical spectrum-resolved transport solution with the chemical evolution (e.g., Gaches et al. 2019; Owen et al. 2021). While Gaches et al. (2019) used the continuously-slowing down approximation, Owen et al. (2021) solved the one-dimensional transport equation, but with a more limited chemical network. The advantage of these methods is that the ionization rates and other processes can be computed directly from the spectrum. Currently, the only public astrochemical code with a one-dimensional spectrum-resolved solution of transport is 3D-PDR[5] (Gaches et al. 2019).
- Multi-dimensional solutions: Astrophysical hydrodynamic codes are beginning to include cosmic-ray transport solvers and reduced chemical networks. While this solves the hydrodynamics and cosmic-ray transport in multi-dimensions with time dependence, the chemical networks are constrained due to numerical expense. Currently, no public astrochemistry codes include multi-dimensional solvers of transport.

8.4 ENERGY LOSS FUNCTION

The quantity that controls the energy degradation of a particle propagating through a medium is the so-called energy loss function, already introduced in Sect. 8.3.2.1. The expression for the partial energy loss function, L_k^l, for a particle of species k depends on the type of process l: if only a small fraction of the particle kinetic energy is lost in each collision with a particle of the medium, the process can be considered continuous and described by the loss function

$$L_k^l(E) = \int_0^{E^{\max}} E' \frac{\mathrm{d}\sigma_k^l(E, E')}{\mathrm{d}E'} \mathrm{d}E' \,, \tag{8.51}$$

where $\mathrm{d}\sigma_k^l/\mathrm{d}E'$ is the differential cross section of the process and $E^{\max}$ is the maximum energy lost in a collision. In the extreme case, where the entire kinetic energy is lost in a single collision or the cosmic-ray particle ceases to exist after the collision, the process is called catastrophic and the loss function becomes

$$L_k^l(E) = E\sigma_k^l(E) \,, \tag{8.52}$$

4. https://uclchem.github.io
5. https://uclchem.github.io/3dpdr

where σ_k^l is the cross section of the process.
For electrons colliding with H_2, it is described by

$$L_e(E) = \frac{2m_e}{m_{H_2}}\sigma_e^{\text{m.t.}}(E)E + \sum_j \sigma_e^{\text{exc},j}(E)E_{\text{thr},j} + \int_0^{(E-I)/2} \frac{\mathrm{d}\sigma_e^{\text{ion}}(E,\varepsilon)}{\mathrm{d}\varepsilon}(I+\varepsilon)\mathrm{d}\varepsilon + \int_0^E \frac{\mathrm{d}\sigma_e^{\text{br}}(E,E_\gamma)}{\mathrm{d}E_\gamma}E_\gamma \mathrm{d}E_\gamma + KE^2 \,. \tag{8.53}$$

Terms on the right-hand side represent the contributions of momentum transfer, rotational, vibrational, and electronic excitation, ionization, and bremsstrahlung. In addition, the last term on the right-hand side represents synchrotron losses that only depend on the strength of the magnetic field in the cloud. Here, m_e and m_{H_2} are the electron and H_2 mass, respectively, $\sigma_e^{\text{m.t.}}$ and $\sigma_e^{\text{exc},j}$ are the cross section of momentum transfer and excitation of state j, $E_{\text{thr},j}$ is the corresponding excitation threshold energy, $\mathrm{d}\sigma_e^{\text{ion}}/\mathrm{d}\varepsilon$ is the differential ionization cross section (Kim et al. 2000), where ε is the secondary electron energy and I is the ionization threshold, $\mathrm{d}\sigma_e^{\text{br}}/\mathrm{d}E_\gamma$ is the differential bremsstrahlung cross section (Blumenthal & Gould 1970), where E_γ is the energy of the emitted photon. Finally, KE^2 represents synchrotron losses with $K = 5 \times 10^{-38}$ eV cm^2 and E in eV (Schlickeiser 2002). Here we assume the relationship between the magnetic field strength and the volume density given by Crutcher (2012), $B = B_0(n/n_0)^\kappa$, with $B_0 = 10\,\mu$G, $n_0 = 150\,\text{cm}^{-3}$, and $\kappa = 0.5-0.7$. We choose $\kappa = 0.5$ to remove the dependence on n (see Padovani et al. 2018b, for details). For completeness, depending on the temperature and on the ionization fraction of the medium, one has to account for Coulomb losses, L_C that reads (Swartz et al. 1971)

$$L_e^\text{C}(E) = 2\times 10^4 \frac{x_e}{v_e E^{0.44}}\left(\frac{E-E_\text{th}}{E-0.53E_\text{th}}\right)^{2.36} \text{eV cm}^2\,, \tag{8.54}$$

where x_e is the electron fraction, v_e is the electron velocity, and $E_\text{th} = k_\text{B}T$ is the electron thermal energy, where k_B is the Boltzmann constant and T is the temperature. For example, in starless cores, with typical temperatures ($T \simeq 10$ K) and ionisation fractions ($x_e < 10^{-7}$), Coulomb losses dominate below $\simeq 0.3$ eV; in protostellar shocks, assuming, e.g. $T \simeq 10^4$ K and $x_e \simeq 0.01$, Coulomb losses prevail below $\simeq 20$ eV.

Similarly, for protons colliding with H_2, the energy loss function is given by

$$L_p(E) = \frac{2m_p m_{H_2}}{(m_p + m_{H_2})^2}\sigma_p^{\text{m.t.}}(E)E + \sum_j \sigma_p^{\text{exc},j}(E)E_{\text{thr},j} + (I + \langle\varepsilon\rangle)\frac{\sigma_p^{\text{e.c.}}\sigma_{\text{H}}^{\text{self-ion}}}{\sigma_p^{\text{e.c.}} + \sigma_{\text{H}}^{\text{self-ion}}} + \int_0^{4m_e E/m_p} \frac{\text{d}\sigma_p^{\text{ion}}(E,\varepsilon)}{\text{d}\varepsilon}(I + \varepsilon)\text{d}\varepsilon + L_p^{\pi}(E)\,. \tag{8.55}$$

On the right-hand side, in addition to the momentum transfer, excitation, and ionization terms already described in Eq. (8.53), there are losses due to electron capture and to pion production. The expression for the energy loss by electron capture can be derived following Edgar et al. (1973); Miller & Green (1973); Edgar et al. (1975). The following cycle must be considered

$$\text{p} + \text{H}_2 \rightarrow \text{H}_{\text{fast}} + \text{H}_2^+$$
$$\text{H}_{\text{fast}} + \text{H}_2 \rightarrow \text{p} + \text{H}_2 + \text{e}^-\,.$$

In the first process the ionization energy of H_2, I, is lost, while in the second the average energy of the ejected electron, $\langle\varepsilon\rangle$, is lost. Thus the contribution of the electron capture cycle to the loss function is

$$L_p^{\text{e.c.}} = f_p I\sigma_p^{\text{e.c.}} + f_{\text{H}}\langle\varepsilon\rangle\sigma_{\text{H}}^{\text{self-ion}}\,, \tag{8.56}$$

where f_p and f_{H} are given in Sect. 8.5.3 and

$$\langle\varepsilon\rangle = \varepsilon_0 - \frac{\varepsilon_{\max}}{\exp(\varepsilon_{\max}/\varepsilon_0) - 1}\,. \tag{8.57}$$

Here, $\varepsilon_{\max} = 4(m_e/m_p)E$ is the maximum energy of the ejected secondary electron corresponding to an incident proton of energy E and ε_0 is the secondary saturation energy, adjusted to reproduce the experimental data, which is set to 20 eV.

The expression for pion losses, L_p^{π}, whose contribution becomes important and then dominant above 280 MeV, is given by (Krakau & Schlickeiser 2015)

$$L_p^{\pi}(E) = \frac{1.5\times10^{-16}}{\beta c}E^{1.28}(E + 2\times10^{11})^{-0.2}\ \text{eV cm}^2\,, \tag{8.58}$$

where $\beta = \gamma^{-1}\sqrt{\gamma^2 - 1}$ and γ is the Lorentz factor.

As for electrons, depending on the temperature and on the ionization fraction, Coulomb losses must be included and are given by Mannheim & Schlickeiser (1994)

$$L_p^{\text{C}}(E) = \frac{3.1\times10^{-7}}{\beta c}\frac{x\beta^2}{\beta_{\text{th}}^3 + \beta^3}\ \text{eV cm}^2\,, \tag{8.59}$$

where $\beta_{\text{th}} = 2\times10^{-5}\sqrt{T/\text{K}}$.

8.5 COSMIC-RAY INTERACTION CROSS SECTIONS

Cosmic rays (protons, electrons, and heavy nuclei) play a key role in ionization, excitation, dissociation, and spallation processes of atoms and molecules of the interstellar medium. In this section, we summarize the main reactions involving H_2 and He as targets. We present some useful parameterizations for coding by referring to the main publications and available public databases. Tab. 8.3 lists the main reactions triggered by CR electrons, protons, and fast H atoms produced by proton-electron capture. For the momentum transfer, pure rotational, and pure vibrational cross sections of $H + H_2$ we refer to the parameterizations given by Tabata & Shirai (2000).

8.5.1 Cosmic-ray electron reactions with H_2

If the energy of a CR electron is lower than 15.426 eV, which is the energy needed to ionize a hydrogen molecule, there is a transfer of momentum or H_2 will be excited or dissociated. The momentum transfer cross section has been studied for many decades both experimentally and theoretically (Shyn & Sharp 1981; Nishimura et al. 1985; Khakoo & Trajmar 1986; England et al. 1988; Brunger et al. 1990, 1991; Schmidt et al. 1994; Dalgarno et al. 1999). Here we adopt the parameterization by Pinto & Galli (2008) given by

$$\frac{\sigma}{a_0^2} = c_0 \frac{(E + c_1)^{c_2}}{(E + c_3)^{c_4}} , \tag{8.60}$$

where $a_0 \simeq 5.2918 \times 10^{-9}$ cm is the Bohr radius, E is the electron energy in eV, and the coefficients c_k are given in Tab. 8.4. H_2 excitation induced by electrons is a well-studied process both from experimental (e.g. Hall & Andric 1984; Khakoo & Trajmar 1986; Mason & Newell 1986; Nishimura & Danjo 1986; Khakoo et al. 1987; Khakoo & Segura 1994; Wrkich et al. 2002; Kato et al. 2008; Hargreaves et al. 2017; Zawadzki et al. 2018) and theoretical (e.g. Dalgarno et al. 1999; Janev et al. 2003; Yoon et al. 2008; Liu et al. 2017; Padovani et al. 2022) perspective.

The purely rotational excitation cross section, $J = 0 \rightarrow 2$, has been recently revised by Scarlett et al. (2021), finding a good agreement with England et al. (1988). It can be parameterized by the sum of two polynomials of the form

$$\log \frac{\sigma}{a_0^2} = \sum_k c_k \log^k \left(\frac{E}{\mathrm{eV}} \right) . \tag{8.61}$$

The coefficients c_k are listed in Tab. 8.4.

The purely vibrational excitation of H_2 has been studied by Ehrhardt et al. (1968), Linder & Schmidt (1971)., Nishimura et al. (1985), Brunger et al. (1991), Dalgarno et al. (1999), Janev et al. (2003), Yoon et al. (2008), and Scarlett et al. (2019). In its ground electronic state, $X\,^1\Sigma_g{}^+$, it takes place through two different

		Reaction	Process	Symbol
H_2 target	►	$e^- + H_2 \rightarrow e^- + H_2$	momentum transfer	$\sigma_e^{m.t.}$
	►	$e^- + H_2 \rightarrow e^- + H_2^*$	excitation	σ_e^{exc}
	►	$e^- + H_2 \rightarrow e^- + H + H$	dissociation	σ_e^{diss}
	►	$e^- + H_2 \rightarrow e^- + H_2^+ + e^-$	ionization	σ_e^{ion}
		$e^- + H_2 \rightarrow e^- + H + H^+ + e^-$	dissociative ionization	$\sigma_e^{diss.ion.}$
		$e^- + H_2 \rightarrow e^- + 2H^+ + 2e^-$	double ionization	$\sigma_e^{doub.ion.}$
	►	$p + H_2 \rightarrow p + H_2$	momentum transfer	$\sigma_p^{m.t.}$
	►	$p + H_2 \rightarrow p + H_2^*$	excitation	σ_p^{exc}
		$p + H_2 \rightarrow p + H + H$	dissociation	σ_p^{diss}
	►	$p + H_2 \rightarrow p + H + H^*(n=2)$	dissociative excitation	$\sigma_p^{Ly-\alpha}$
	►	$p + H_2 \rightarrow p + H + H^*(n=3)$	dissociative excitation	$\sigma_p^{H\alpha}$
	►	$p + H_2 \rightarrow p + H_2^+ + e^-$	ionization	σ_p^{ion}
	►	$p + H_2 \rightarrow H_2^+ + H_{fast}$	electron capture	$\sigma_p^{e.c.}$
		$p + H_2 \rightarrow p + H + H^+ + e^-$	dissociative ionization	$\sigma_p^{diss.ion.}$
		$p + H_2 \rightarrow p + 2H^+ + e^-$	double ionization	$\sigma_p^{doub.ion.}$
		$H_{fast} + H_2 \rightarrow H_{fast} + H_2$	momentum transfer	$\sigma_H^{m.t.}$
		$H_{fast} + H_2 \rightarrow H_{fast} + H + H$	dissociation	σ_H^{diss}
	►	$H_{fast} + H_2 \rightarrow H_{fast} + H_2^+ + e^-$	ionization	σ_H^{ion}
	►	$H_{fast} + H_2 \rightarrow p + H_2 + e^-$	self-ionization	$\sigma_H^{self-ion}$
He target	►	$e^- + He \rightarrow e^- + He$	momentum transfer	$\sigma_e^{m.t.}$
	►	$e^- + He \rightarrow e^- + He^*$	excitation	σ_e^{exc}
	►	$e^- + He \rightarrow e^- + He^+ + e^-$	ionization	σ_e^{ion}
	►	$p + He \rightarrow p + He$	momentum transfer	$\sigma_p^{m.t.}$
	►	$p + He \rightarrow p + He^*$	excitation	σ_p^{exc}
	►	$p + He \rightarrow p + He^+ + e^-$	ionization	σ_p^{ion}
	►	$p + He \rightarrow H + He^+$	electron capture	$\sigma_p^{e.c.}$

TABLE 8.3 Main cosmic-ray reactions with H_2 and He. To simplify the notation, we omit the target molecule (H_2, He) in the subscript of the symbols' column. Black right-pointing triangles identify the most important reactions that are discussed in more detail in the text.

two-step processes: via the H_2^- resonant state

$$e^- + H_2(v) \rightarrow e^- + H_2^-(X^2\Sigma_u^+, B^2\Sigma_g^+) \rightarrow e^- + H_2(v')\,,\ v' > v$$

and via the electronic excited states, $H_2^*(N^1\Lambda_u)$,

$$e^- + H_2(v) \rightarrow e^- + H_2^*(N^1\Lambda_u; v'') \rightarrow e^- + H_2(v') + h\nu\,,\ N \geq 2\,, v' > v\,,$$

whose major contributions come from the two lowest excited states, $B^1\Sigma_u^+$ and $C^1\Pi_u$. The fit for the $v = 0 \rightarrow 1$ and $v = 0 \rightarrow 2$ cross sections via H_2^- is given by (Janev et al. 2003)

$$\frac{\sigma}{a_0^2} = \frac{c_0}{\Delta E^4}\frac{1}{x^2}\left(1 - \frac{1}{x}\right)^{c_1/\sqrt{\Delta E}}\,. \tag{8.62}$$

The fit for the vibrational cross sections via electronic excited states is given by (Scarlett et al. 2019) and is parameterized by

$$\frac{\sigma}{a_0^2} = \frac{x-1}{x}\left(c_0^2\frac{\ln x}{x} + \frac{c_1}{x} + \frac{c_2}{x^2} + \frac{c_3}{x^3} + \frac{c_4}{x^4} + \frac{c_5}{x^5}\right)\,. \tag{8.63}$$

In the two above equations, $x = E/\Delta E$, E is the electron energy, ΔE is the threshold energy, and the coefficients c_k are given in Tab. 8.4.

For the electronic excitation cross sections, we focus on the most up-to-date and accurate results for direct use by Scarlett et al. (2021), calculated using the molecular convergent close-coupling (MCCC) method. Data are accessible through a web database[6] for the excitation of any vibrational level of the H_2 ground electronic state $X^1\Sigma_g^+$ to any vibrational level of the singlet ($B^1\Sigma_u^+$, $C^1\Pi_u$, $EF^1\Sigma_g^+$, $B'^1\Sigma_u^+$, $GK^1\Sigma_g^+$, $I^1\Pi_g$, $J^1\Delta_g$, $D^1\Pi_u$, and $H^1\Sigma_g^+$) and triplet ($b^3\Sigma_u^+$, $a^3\Sigma_g^+$, $c^3\Pi_u$, $e^3\Sigma_u^+$, $h^3\Sigma_g^+$, $d^3\Pi_u$, $g^3\Sigma_g^+$, $i^3\Pi_g$, and $j^3\Delta_g$) states. Here we give the parameterizations for the excitation cross sections from the lowest vibrational ($v = 0$) level of the ground state summed over all the final vibrational levels of the final state, which are useful for most applications and for building the energy loss function (see Sect. 8.4). Singlet cross sections are parameterized by Eq. (8.63). Triplet cross sections, except for the $b^3\Sigma_u^+$ state, are parameterized by

$$\frac{\sigma}{a_0^2} = \frac{x-1}{x}\left(\frac{c_0^2}{x} + \frac{c_1}{x^2} + \frac{c_2}{x^3} + \frac{c_3}{x^4} + \frac{c_4}{x^5}\right)\,. \tag{8.64}$$

Finally, the fit for the triplet $b^3\Sigma_u^+$ state reads

$$\frac{\sigma}{a_0^2} = \frac{c_0}{(x-1)^{c_1^2}}\exp\left[-\frac{c_2}{(x-1)^{c_3}}\right]\,. \tag{8.65}$$

6. https://mccc-db.org

All the coefficients c_k are given in Tab. 8.4.
Every singlet and triplet state partly contributes to the dissociation process, except for the triplet $b^3\Sigma_u^+$ state that is fully dissociative. We parameterize the H_2 dissociation cross section by electron impact with two fits that must be summed to obtain the total cross section. These fits account for the singlet and triplet contributions to the dissociation cross section and are parameterized by Eq. (8.63) and Eq. (8.65), respectively. We note that the two parameterizations have different threshold energies, as listed in Tab. 8.4.
The accurate expression of the $e^- + H_2$ ionization cross section is given by Kim et al. (2000). The latter must be derived from integrating the differential ionization cross section, which has a complicated form. Thus, we provide for convenience a parameterization of its non-relativistic component following the semi-empirical model by Rudd (1991)

$$\frac{\sigma}{a_0^2} = 4\pi c_0 F(x) G(x)\,, \tag{8.66}$$

where

$$F(x) = \frac{1 - x^{1-c_1}}{c_1 - 1} - \left(\frac{2}{1+x}\right)^{c_1/2} \frac{1 - x^{1-c_1/2}}{c_1 - 2} \tag{8.67}$$

and

$$G(x) = \frac{c_2 \ln x + c_3 + c_4/x}{x}\,. \tag{8.68}$$

Here, $x = E/\Delta E$, where ΔE is the H_2 ionization threshold. The relativistic correction, to be added to Eq. (8.66), is parameterized with a polynomial fit given by Eq. (8.61), whose coefficients are listed in Tab. 8.4. The total ionization cross section is given by the sum of the two latter expressions. We point out that the inclusion of the relativistic component is crucial for the proper calculation of the energy loss function and then for the evaluation of the cosmic-ray flux at a given column density.
Dissociative ionization and double ionization are secondary processes. Their contribution to ionization is at least an order of magnitude lower than direct ionization. For more details, we refer to Sect. 3 of Padovani et al. (2009), where the parameterizations for these reactions are also available. Fig. 8.5 shows the cross sections described in the text.

8.5.2 Cosmic-ray proton reactions with H_2

The momentum transfer cross section for proton colliding with H_2 has been studied by Bachmann & Reiter (1995), Krstić & Schultz (1999), Phelps (1990), and Pinto & Galli (2008). We parameterize it with two polynomial fits (Eq. (8.61)) at low and high energies. The rotational $J = 0 \rightarrow 2$ cross section is based on experimental data by Linder (1980) and the calculation by Gianturco & Tritella (1977), and it can be parameterized by a polynomial fit (Eq. (8.61)). The coefficients for both the momentum transfer and the rotational cross sections are

	cross section	ΔE [eV]	c_0	c_1	c_2	c_3	c_4	c_5	Eq.
	momentum transfer		4.64(5)	7.30(−2)	4.10(−1)	1.20(1)	3.50		(8.60)
	rotational, J = 0 → 2 (P1)		1.600(−1)	1.190(−1)	−2.970	−4.084	−1.734		(8.61)
	rotational, J = 0 → 2 (P2)		5.000(−3)	2.938	−3.380	1.190	1.510(−1)		(8.61)
	vibrational (H_2^-), v = 0 → 1	0.516	2.064(1)	6.11					(8.62)
	vibrational (H_2^-), v = 0 → 2	1.003	1.296(1)	6.11					(8.62)
	vibrational (H_2^*), v = 0 → 1	1.11828(1)	7.87747(−1)	1.29437	−8.82256	2.17800(1)	−2.24449(1)	8.18214	(8.63)
	vibrational (H_2^*), v = 0 → 2	1.11828(1)	7.23614(−1)	1.12837	−7.72425	1.88284(1)	−1.89415(1)	6.66888	(8.63)
$X^1\Sigma_g^+ \to$ singlet state	$B^1\Sigma_u^+$	1.11829(1)	2.280	1.736	−1.982(1)	4.978(1)	−4.429(1)	1.237(1)	(8.63)
	$C^1\Pi_u$	1.22910(1)	2.089	4.556	−3.321(1)	7.742(1)	−7.332(1)	2.480(1)	(8.63)
	$EF^1\Sigma_g^+$	1.23000(1)	5.732(−1)	1.909(−1)	2.683	−1.357(1)	2.410(1)	−1.237(1)	(8.63)
	$B'^1\Sigma_u^+$	1.36960(1)	7.576(−1)	9.710(−1)	−4.765	9.642	−8.196	2.388	(8.63)
	$GK^1\Sigma_g^+$	1.37896(1)	1.917(−1)	−7.219(−2)	6.560(−1)	−1.556	1.896	−8.322(−1)	(8.63)
	$I^1\Pi_g$	1.38805(1)	−2.631(−5)	1.067(−1)	9.701(−2)	−1.712(−1)	−2.940(−2)	−2.284(−2)	(8.63)
	$J^1\Delta_g$	1.39389(1)	1.953(−1)	−7.138(−2)	8.507(−1)	−2.274	3.169	−1.545	(8.63)
	$D^1\Pi_u$	1.40070(1)	8.470(−1)	1.436	−8.190	1.763(1)	−1.627(1)	5.435	(8.63)
	$H^1\Sigma_g^+$	1.40115(1)	4.042(−1)	−3.240(−1)	2.022	−4.909	6.022	−2.755	(8.63)
$X^1\Sigma_g^+ \to$ triplet state	$b^3\Sigma_u^+$	4.47713	7.143	1.317	4.187	3.746			(8.65)
	$a^3\Sigma_g^+$	1.17934(1)	−2.873(−4)	−4.378(−1)	5.776	−1.389(1)	1.598(1)		(8.64)
	$c^3\Pi_u$	1.17706(1)	−9.084(−5)	1.781	−7.874	2.423(1)	−1.514(1)		(8.64)
	$e^3\Sigma_u^+$	1.32260(1)	8.298(−5)	6.750(−1)	−4.047	9.877	−5.999		(8.64)
	$h^3\Sigma_g^+$	1.38434(1)	−2.231(−5)	2.320(−1)	−8.670(−1)	1.010	1.056		(8.64)
	$d^3\Pi_u$	1.38553(1)	−1.924(−7)	4.148(−1)	−2.059	5.601	−3.168		(8.64)
	$g^3\Sigma_g^+$	1.38876(1)	−1.105(−6)	5.002(−2)	−2.549(−1)	5.990(−1)	−2.538(−1)		(8.64)
	$i^3\Pi_g$	1.38797(1)	1.519(−5)	8.892(−2)	−4.651(−1)	1.109	−5.099(−1)		(8.64)
	$j^3\Delta_g$	1.39379(1)	−2.541(−6)	8.624(−2)	−4.966(−1)	1.187	−6.275(−1)		(8.64)
	dissociation (s)	1.11828(1)	2.90372(−3)	9.38358	−4.53047(1)	1.02623(2)	−1.0969(2)	4.30868(1)	(8.63)
	dissociation (t)	4.47709	4.16152(2)	1.79158	7.67185	1.35658			(8.65)
	ionization (NR)	1.5426(1)	1.55	2.40	0.74	0.87	−0.60		(8.66)
	ionization (R)		−6.40283	1.27737	−1.24050(−1)	4.20000(−3)			(8.61)

TABLE 8.4 Fitting coefficients for the H_2 momentum transfer, purely rotational, purely vibrational, electronic excitation, dissociation, and ionization cross sections by electron impact. Fits are valid in the energy range $0.05 - 10^3$ eV for the rotational J = 0 → 2, from the threshold energy up to 500 eV for the singlet states, up to 150 eV for the triplet $b^3\Sigma_u^+$ state, up to 50 eV for all the other triplet states, in the energy range $8 - 100$ eV for dissociation, and below 0.1 TeV for ionization. Labels s and t stand for singlet and triplet contributions to the dissociation cross section. Labels NR and R stand for non-relativistic ionization cross section and its relativistic correction, respectively. The two latter parameterizations must be summed to obtain the total ionization cross section. Numbers in brackets indicate the power of ten, e.g. $m(n) = m \times 10^n$. The rightmost column displays the reference equation.

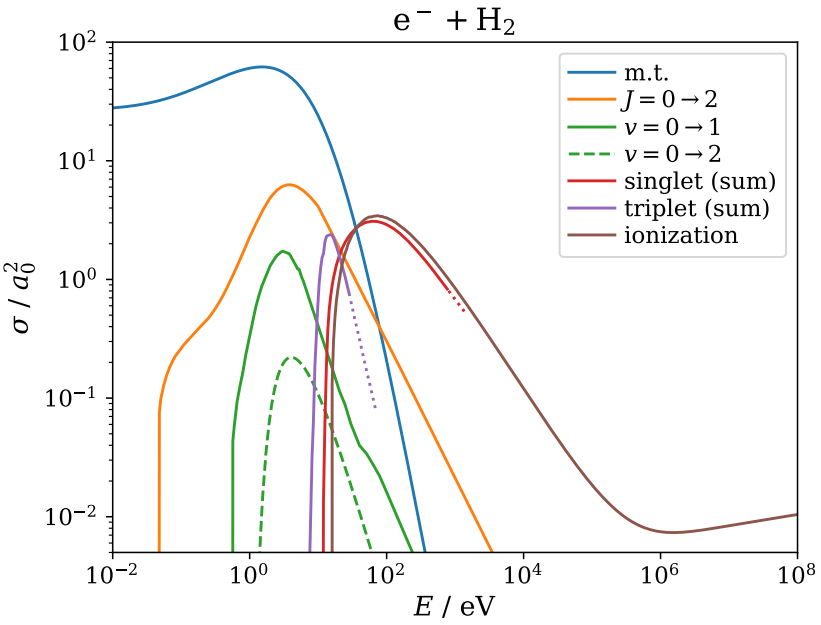

FIGURE 8.5 Main cross sections for electrons colliding with H_2. Singlet and triplet electronic cross sections are summed over all the corresponding states (see Tab. 8.4 for details).

given in Tab. 8.5. The vibrational cross section has been theoretically obtained among others by Gentry & Giese (1975) and Schinke (1977) and experimentally by Niedner et al. (1987) and Herrero & Doering (1972). Janev et al. (2003) gives the following parameterization

$$\sigma = \sigma_- + \sigma_+ , \tag{8.69}$$

where

$$\frac{\sigma_-}{a_0^2} = \frac{c_0 \exp(-c_1/E^{c_2})\chi(E-\Delta E)}{E^{c_3}} , \tag{8.70}$$

and

$$\frac{\sigma_+}{a_0^2} = \frac{c_0 \exp(-c_1/E^{c_2})}{E^{c_3}(1+c_4 E^{c_5})} , \tag{8.71}$$

where $\chi(E-\Delta E) = 0$ for $E < E_0$, otherwise it is equal to 1. All the coefficients are given in Tab. 8.5.

The proton impact induced dissociation of H_2 in the ground state and for the lowest vibrational level has been parameterized by Janev et al. (2003) as

$$\frac{\sigma}{a_0^2} = \frac{c_0}{E^{c_1}} \left[1 - \left(1.5 \frac{\Delta E}{E} \right)^{c_2} \right]^{c_3} , \tag{8.72}$$

whose coefficients are given in Tab. 8.5. It peaks at around 8.48 eV, but it is negligible with respect to the rotational $J = 0 \rightarrow 2$ and the vibrational $v = 0 \rightarrow 1$ cross sections at the same energy. However, if the proton energy is high enough, in the process of H_2 dissociation, one of the two H atoms is excited. The latter can be a source for Lyman-α and Hα radiation. The Lyman-α cross section has been studied by van Zyl et al. (1967, 1989); Phelps (1990) and the Hα (also known as Balmer-α) cross section by Williams et al. (1982). Both can be parameterized by summing two polynomials (Eq. (8.61)).

No studies have been conducted so far for H_2 electronic excitation by proton impact. However, based on the results obtained for proton-hydrogen atom excitation collisions, these processes are expected to be negligible with respect to excitation by electron impact (Janev et al. 2003). Likewise, H_2 dissociation by proton impact is a negligible process. This is because the proton flux at the energies where excitation and dissociation cross sections peak ($E \approx 10$ eV), is much lower than the electron flux at the same energies (see e.g. Sect. 2 in Padovani et al. 2018a and Sect. 2.3 in Padovani et al. 2022 for more details).

For the $p + H_2$ ionization cross section, we adopt the analytical expression for the differential cross section by Rudd (1988) corrected for relativistic proton energies following by Krause et al. (2015), then integrated in energy. After integration in energy, the total ionization cross section turns out to be constant for $E \gg m_p c^2$, whereas it should increase logarithmically in energy. However, the resulting uncertainty is negligible. Analogously to what we have done for the $e^- + H_2$ ionization cross section, we provide the parameterizations of the non-relativistic cross section and its relativistic correction that must be summed up together. For the non-relativistic part, we adopt the fit by Rudd et al. (1985)

$$\frac{\sigma}{a_0^2} = \frac{4\pi}{\sigma_l^{-1} + \sigma_h^{-1}}\,, \tag{8.73}$$

where $\sigma_l = c_0 x^{c_1}$ and $\sigma_h = [c_2 \ln(1 + x) + c_3]/x$. Here $x = (m_e/m_p)(E/\mathrm{Ry})$, where m_e and m_p are the electron and proton mass, respectively, and 1 Ry = 13.6057 eV is the Rydberg energy unit. The relativistic correction is modeled by a polynomial fit as in Eq. (8.61). All the parameters are given in Tab. 8.5.

The electron capture is a charge-exchange process taking place at low energies (the peak of the cross section is at around 7 keV) that is crucial for the neutralization of cosmic-ray protons and the creation of a flux of fast hydrogen atoms (see Sect. 8.5.3). This process has been studied over time by many groups, both experimentally and theoretically (Gilbody & Hasted 1957; Curran et al. 1959; De Heer et al. 1966; Toburen & Wilson 1972; Rudd et al. 1983; Gealy & van Zyl 1987; Baer et al. 1988; Phelps 1990; Errea et al. 2010) and can be parameterized by summing two polynomials, Eq. (8.61). The c_k coefficients are given in Tab. 8.5.

Dissociative and double ionization are negligible processes, as for $e^- + H_2$ collisions. However, the associated cross sections can be assumed equal to the corresponding cross sections for electrons of equal velocity (see Padovani et al.

(2009))

$$\sigma_{\rm p}(E_{\rm p}) = \sigma_{\rm e}(E_{\rm e} = m_{\rm e}E_{\rm p}/m_{\rm p})\,, \tag{8.74}$$

where $E_{\rm p}$ and $E_{\rm e}$ are the proton and electron energies, respectively. Fig. 8.6 shows the cross sections described in the text.

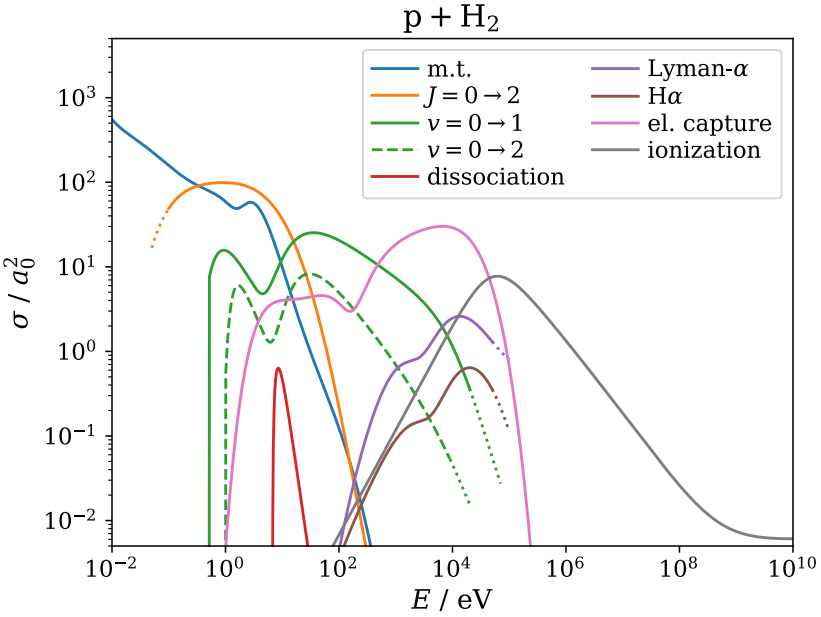

FIGURE 8.6 Main cross sections for protons colliding with H_2 (see Tab. 8.5 for details).

8.5.3 Fast hydrogen atom reactions with H_2

Fast hydrogen atoms are created by the electron capture process during the collision between cosmic-ray protons and H_2. Through this process, a cosmic-ray proton is neutralized, and the newly formed hydrogen atom gets most of the initial kinetic energy of the proton. This explains the reason for the term "fast". The flux of fast H atoms can, in turn, dissociate and ionize H_2, but it is a negligible process compared to the dissociation caused by electrons (see Fig. 3 in Padovani et al. 2018a). As shown below, H_2 ionization by H can play a fairly prominent role in some cases. First, we need to introduce the reverse process to electron capture, namely the self-ionization whereby the hydrogen atom separates into $p + e^-$ (see Tab. 8.3). Measurements for H self-ionization have been carried out by Stier & Barnett (1956), van Zyl et al. (1981), and Phelps (1990). Since the resulting cross section is double-peaked, we parameterize it by the sum of two polynomials, both given by Eq. (8.61). The two sets of coefficients c_k are given in Tab. 8.6.

cross section	ΔE [eV]	c_0	c_1	c_2	c_3	c_4	c_5	Eq.
momentum transfer (low)		1.7675	−0.6688	−1.1908	−1.7253	−0.9610	−0.1867	(8.61)
momentum transfer (high)		−0.3499	9.8771	−15.8206	9.8114	−2.8174	0.2987	(8.61)
rotational, J = 0 → 2		1.996	−0.017	−0.202	−0.095	−0.166	0.050	(8.61)
vibrational (σ_-), v = 0 → 1	0.51598	2.5747(1)	0.50	2.15	1.255			(8.70)
vibrational (σ_-), v = 0 → 2	1.00273	2.0391(1)	3.75	4.50	1.65			(8.70)
vibrational (σ_+), v = 0 → 1		2.2140(2)	26.5	1.15	0.488	1.26(−7)	1.74	(8.71)
vibrational (σ_+), v = 0 → 2		3.0282(2)	60.2	1.32	0.862	8.55(−5)	1.05	(8.71)
dissociation, v = 0	4.478	2.685(4)	4.64	5.37	2.18			(8.72)
Lyman-α (P1)		−2.09583(1)	2.09487(1)	−9.80980	2.56080	−2.83800(−1)		(8.61)
Lyman-α (P2)		1.99601(1)	−3.69480(1)	1.87189(1)	−3.67580	2.49900(−1)		(8.61)
Hα (P1)		−2.11816(1)	2.60729(1)	−1.45601(1)	3.90170	−3.99900(−1)		(8.61)
Hα (P2)		6.21700	−2.15327(1)	1.12799(1)	−2.07550	1.24700(−1)		(8.61)
ionization (NR)		0.51	1.24	0.71	1.63			(8.73)
ionization (R)		−3.4481(1)	1.0789(1)	−1.3539	7.5571(−2)	−1.5831(−3)		(8.61)
electron capture (low)		−2.34180	9.29230	−1.09282(1)	5.66420	−1.08250		(8.61)
electron capture (high)		−3.54216(1)	4.03580(1)	−1.69718(1)	3.23650	−2.34900(−1)		(8.61)

TABLE 8.5 Fitting coefficients for the H_2 momentum transfer, purely rotational and vibrational, Lyman-α, ionization and electron capture cross sections by proton impact. The parameterizations for momentum transfer and electron capture at low and high energies, for vibrational transition (σ_- and σ_+), for Lyman-α and Hα (P1 and P2), and for non-relativistic ionization cross section (NR) and its relativistic correction (R) must be summed to obtain the total cross section. The momentum transfer, rotational, Lyman-α, Hα, relativistic cross sections, and electron capture are valid for energies between 0.01 and 400 eV, between 0.1 and 300 eV, between 100 eV and 100 keV (for both Lyman-α and Hα), below 0.1 TeV, and above 2 eV, respectively. Numbers in brackets indicate the power of ten, e.g. $m(n) = m \times 10^n$. The rightmost column displays the reference equation.

cross section	c_0	c_1	c_2	c_3	c_4	Eq.
self-ionization (P1)	1.00014(1)	−1.62369(1)	7.04180	−9.07400(−1)		(8.61)
self-ionization (P2)	−4.27082(1)	2.45049(1)	−4.48450	2.63300(−1)		(8.61)
ionization (P1)	−5.60032(1)	9.75746(1)	−6.57428(1)	1.98974(1)	−2.27540	(8.61)
ionization (P2)	−1.4039(1)	7.2978	−1.0483	3.5400(−2)		(8.61)

TABLE 8.6 Fitting coefficients for the H + H_2 self-ionization and ionization cross sections. The parameterizations labeled P1 and P2 must be summed to obtain the corresponding total cross section. Fits are valid in the range 100 eV - 1 MeV and 30 eV - 1 MeV for self-ionization and ionization, respectively. Numbers in brackets indicate the power of ten, e.g. $m(n) = m \times 10^n$. The rightmost column displays the reference equation.

Both electron capture and self-ionization are catastrophic processes, since the respective projectile particles disappear after collisions, and the equilibrium ratio of fast H atoms and protons can be approximated by the ratio of the two cross sections of the above processes, namely

$$\frac{j_{\mathrm{H_{fast}}}}{j_{\mathrm{p}}} \approx \frac{\sigma_{\mathrm{p}}^{\mathrm{e.c.}}}{\sigma_{\mathrm{H}}^{\mathrm{self-ion}}} \,. \tag{8.75}$$

This allows computing the fractions of H atoms

$$f_{\mathrm{H_{fast}}} = \frac{j_{\mathrm{H_{fast}}}}{j_{\mathrm{H_{fast}}} + j_{\mathrm{p}}} = \frac{\sigma_{\mathrm{p}}^{\mathrm{e.c.}}}{\sigma_{\mathrm{p}}^{\mathrm{e.c.}} + \sigma_{\mathrm{H}}^{\mathrm{self-ion}}} \tag{8.76}$$

and of protons, $f_{\mathrm{p}} = 1 - f_{\mathrm{H_{fast}}}$. The expressions for f_{p} and f_{H} are required to calculate the energy loss due to electron capture (see Sect. 8.4).
Fig. 8.7 shows that for energies below $\approx$ 10 keV, only less than 10% of non-molecular hydrogen is in the form of protons. This means that H_2 ionization at these energies is determined by collision with fast H atoms. As for the self-ionization of H, also the ionization of H_2 by H impact cross section is double-peaked. Based on the measurements carried out by van Zyl et al. (1981), we parameterize it by the sum of two polynomials, both given by Eq. (8.61). The two sets of coefficients c_k are given in Tab. 8.6.

8.5.4 Cosmic-ray electron reactions with He

Helium is the second most abundant element of the interstellar medium. In this section, we discuss the most important processes involving the collisions between cosmic rays and He atoms.
Helium momentum transfer cross section has been obtained experimentally by Crompton et al. (1967, 1970); Milloy & Crompton (1977); Ramanan & Freeman (1990). Here we adopt the parameterization by Pinto & Galli (2008), given by Eq. (8.60). Helium excitation and ionization by electrons have been extensively studied from both theoretical and experimental sides (e.g. Kato et al. 1992; de

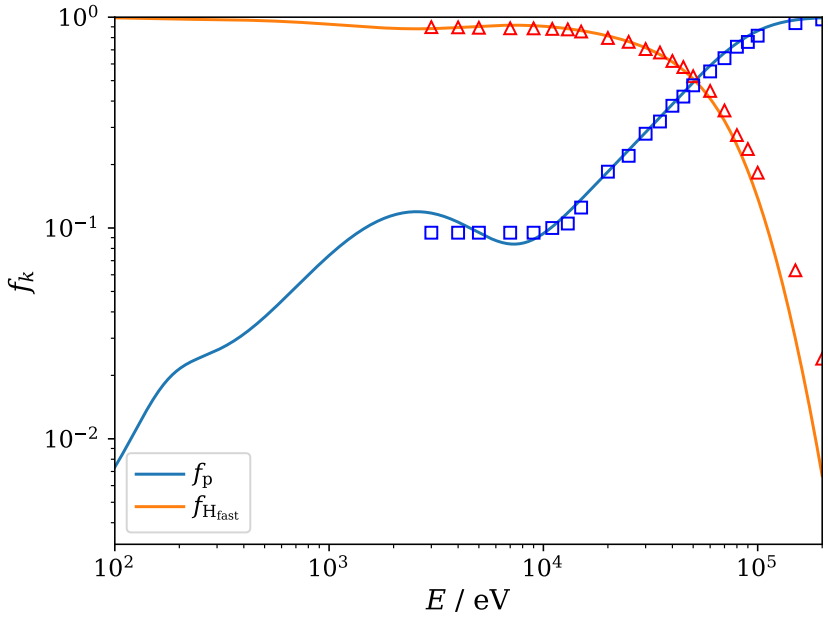

FIGURE 8.7 Fraction of non-molecular hydrogen in neutral ($f_{\mathrm{H_{fast}}}$) and ionised (f_{p}) form as a function of the energy. Experimental data (blue squares and red triangles) from Allison (1958).

Heer 1998; Beigman et al. 2000; Fursa & Bray 2003; Uhlmann et al. 2005). Ralchenko et al. (2008) critically assessed the available data and presented analytic fits for the excitation cross sections. Here we summarize the main processes for the excitation of ground parahelium state 1^1S for the dipole-allowed ($\Delta S = 0, \Delta L = \pm 1$), dipole-forbidden ($\Delta S = 0, \Delta L \neq \pm 1$), and spin-forbidden ($\Delta S \neq 0$) transitions. Here, ΔS and ΔL are the variations of the total electron spin and the total angular momentum, respectively. Cross sections are parameterized by

$$\frac{\sigma}{a_0^2} = \frac{\pi \mathrm{Ry}}{g_l E} \Omega(x) \,, \tag{8.77}$$

where g_l is the statistical weight of the initial state ($g_l = 1$ for 1^1S), $x = E/\Delta E$, and ΔE is the threshold energy. The collision strength, Ω, is given by

$$\Omega(x) = \left(c_0 \ln x + c_1 + \frac{c_2}{x} + \frac{c_3}{x^2} + \frac{c_4}{x^3} \right) \frac{x+1}{x+c_5} \tag{8.78}$$

for dipole-allowed transitions,

$$\Omega(x) = \left(c_0 + \frac{c_1}{x} + \frac{c_2}{x^2} + \frac{c_3}{x^3} \right) \frac{x^2}{x^2 + c_4} \tag{8.79}$$

for dipole-forbidden transitions, and

$$\Omega(x) = \left(c_0 + \frac{c_1}{x} + \frac{c_2}{x^2} + \frac{c_3}{x^3}\right) \frac{1}{x^2 + c_4} \tag{8.80}$$

for spin-forbidden transitions. Threshold energies, ΔE, and coefficients c_k are given in Tab. 8.7.

The $e^- + He$ ionization cross section, including the correct relativistic trend, is given by Kim et al. (2000). As for $e^- + H_2$, we give the parameterization for its non-relativistic and relativistic components through Eq. (8.66) and Eq. (8.61), respectively. Tab. 8.7 lists the coefficients for the fit.

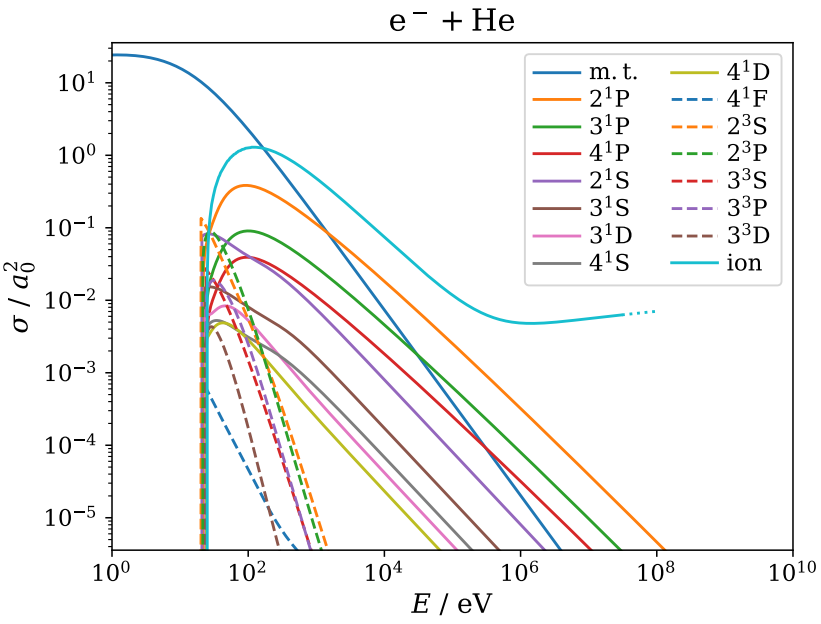

FIGURE 8.8 Main cross sections for electrons colliding with He atoms (see Tab. 8.7 for details).

8.5.5 Cosmic-ray proton reactions with He

A variety of studies have been completed to characterize the excitation of helium by collision with protons, both from the experimental (e.g., Šternberg & Tomaš 1961; Van Eck et al. 1964; Dodd & Hughes 1964; Thomas & Bent 1967; Robinson & Gilbody 1967; Van den Bos et al. 1968; Fritsch 1991) and theoretical point of view (e.g., Vriens 1967; Rodríguez et al. 1997; Dimitriou et al. 2004). In particular, Merabet et al. (2001) showed that He excitation cross sections by proton and electron impact are comparable for equal projectile velocity, Eq. (8.74), if the electron (proton) energy is greater than ≈ 200 eV (≈ 360 keV). However,

	cross section	ΔE [eV]	c_0	c_1	c_2	c_3	c_4	c_5	Eq.
	momentum transfer		9.71(2)	0.03	0.12	13.0	1.4		(8.60)
$1^1S \rightarrow$d.a.	2^1P	2.12182(1)	7.087(−1)	−9.347(−2)	−1.598	2.986	−1.293	3.086(−1)	(8.77),(8.78)
	3^1P	2.30873(1)	1.730(−1)	2.410(−2)	−4.709(−1)	7.690(−1)	−3.216(−1)	8.568(−1)	(8.77),(8.78)
	4^1P	2.37423(1)	6.923(−2)	6.893(−3)	−2.079(−1)	3.508(−1)	−1.497(−1)	4.280(−2)	(8.77),(8.78)
$1^1S \rightarrow$d.f.	2^1S	2.06160(1)	1.888(−1)	−5.754(−1)	3.439	−2.088	2.544(1)		(8.77),(8.79)
	3^1S	2.29206(1)	4.033(−2)	−1.872(−2)	2.368	−1.379	1.258(2)		(8.77),(8.79)
	3^1D	2.30743(1)	9.708(−3)	2.855(2)	−8.265(−2)	4.944(−2)	1.992(−1)		(8.77),(8.79)
	4^1S	2.36738(1)	1.613(−2)	−5.564(−2)	2.943(−1)	−2.024(−1)	2.342(1)		(8.77),(8.79)
	4^1D	2.37366(1)	5.420(−3)	1.198(−2)	−3.173(−2)	1.606(−2)	1.060(−1)		(8.77),(8.79)
	4^1F	2.37373(1)	4.383(−5)	−1.033(−4)	3.772(−3)	1.631(−2)	5.644(1)		(8.77),(8.79)
$1^1S \rightarrow$s.f.	2^3S	1.98198(1)	6.888(−1)	1.975(−1)	7.232	−4.839	5.003(1)		(8.77),(8.80)
	2^3P	2.09643(1)	2.823(−1)	2.048	5.287	−7.363	2.728(1)		(8.77),(8.80)
	3^3S	2.35942(1)	9.392(−2)	−1.641(−1)	7.605(−2)	−4.536(−3)	−9.246(−1)		(8.77),(8.80)
	3^3P	2.37081(1)	6.730(−2)	5.465(−1)	−4.434(−1)	−1.042(−1)	1.140(1)		(8.77),(8.80)
	3^3D	2.30739(1)	2.207(−3)	8.429(−3)	1.816(−1)	−1.812(−1)	9.544		(8.77),(8.80)
	ionization (NR)	2.4587(1)	0.61	2.4	0.85	0.36	−0.10		(8.66)
	ionization (R)		−6.53173	1.27737	−1.24050(−1)	4.20000(−3)			(8.61)

TABLE 8.7 Fitting coefficients for e^- + He momentum transfer, excitation, and ionization cross sections. Fits are valid from the threshold energy up to 10 keV for excitation and up to 0.1 TeV for ionization. Labels d.a., d.f., and s.f. stand for dipole-allowed, dipole-forbidden, and spin-forbidden excitation transition. Labels NR and R stand for non-relativistic and relativistic ionization cross section. The two parameterizations must be summed to obtain the total ionization cross section. Numbers in brackets indicate the power of ten, e.g. $m(n) = m \times 10^n$. The rightmost column displays the reference equation.

cross section	c_0	c_1	c_2	c_3	c_4	Eq.
ionization (NR)	0.13	1.52	0.49	0.62		(8.73)
ionization (R)	−3.5259(1)	1.0789(1)	−1.3539	7.5571(−2)	−1.5831(−3)	(8.61)
electron capture	0.492	0.055	2.850	0.219	5.680	(8.81)

TABLE 8.8 Fitting coefficients for the He ionization and electron capture cross sections by proton impact. Labels NR and R stand for non-relativistic and relativistic ionization cross section. The two parameterizations must be summed to obtain the total ionization cross section. The relativistic cross section is valid for $E < 0.1$ TeV. Numbers in brackets indicate the power of ten, e.g. $m(n) = m \times 10^n$. The rightmost column displays the reference equation.

as anticipated in Sect. 8.5.2, the proton flux at the cross section peak is much lower than that of electrons. Thus, we can safely neglect p + He excitation for our purposes.

For He ionization by proton impact, we use the fit by Rudd et al. (1985) for the non-relativistic part and a polynomial fit for relativistic energies, see Eq. (8.73) and Eq. (8.61), respectively. Finally, for the electron capture we refer to the expression given by Rudd et al. (1983)

$$\frac{\sigma}{a_0^2} = \frac{4\pi c_0 x^2}{c_1 + x^{c_2} + c_3 x^{c_4}}\,, \tag{8.81}$$

where $x = (m_e/m_p)(E/\Delta E)$ and ΔE is the ionization threshold of atomic hydrogen ionization ($\Delta E = 13.598$ eV). All fitting coefficients are given in Tab. 8.8.

BIBLIOGRAPHY

Ackermann, M., Ajello, M., Atwood, W. B., et al. 2010, Phys. Rev. D, 82, 092004

Adriani, O., Barbarino, G. C., Bazilevskaya, G. A., et al. 2011, Phys. Rev. Lett., 106, 201101

Aguilar, M., Aisa, D., Alpat, B., et al. 2015, Phys. Rev. Lett., 114, 171103

Aguilar, M., Aisa, D., Alvino, A., et al. 2014, Phys. Rev. Lett., 113, 121102

Allison, S. K. 1958, Reviews of Modern Physics, 30, 1137

Alves, F. O., Acosta-Pulido, J. A., Girart, J. M., Franco, G. A. P., & López, R. 2011, AJ, 142, 33

Alves, F. O., Franco, G. A. P., & Girart, J. M. 2008, A&A, 486, L13

Alves, F. O., Girart, J. M., Padovani, M., et al. 2018, A&A, 616, A56

Amato, E. & Blasi, P. 2018, Advances in Space Research, 62, 2731

Axford, W. I., Leer, E., & Skadron, G. 1977, in International Cosmic Ray Conference, Vol. 11, International Cosmic Ray Conference, 132

Bacalla, X. L., Linnartz, H., Cox, N. L. J., et al. 2019, A&A, 622, A31

Bachmann, P. & Reiter, D. 1995, Contributions to Plasma Physics, 35, 45

Baer, M., Niedner, G., & Toennies, J. P. 1988, J. Chem. Phys., 88, 1461

Barger, C. J. & Garrod, R. T. 2020, ApJ, 888, 38

Beigman, I. L., Vainshtein, L. A., Brix, M., et al. 2000, Atomic Data and Nuclear Data Tables, 74, 123

Bell, A. R. 1978a, MNRAS, 182, 147

Bell, A. R. 1978b, MNRAS, 182, 443
Bell, A. R. 2013, Astroparticle Physics, 43, 56
Beltrán, M. T., Padovani, M., Girart, J. M., et al. 2019, A&A, 630, A54
Bialy, S. 2020, Communications Physics, 3, 32
Bialy, S., Belli, S., & Padovani, M. 2022, A&A, 658, L13
Black, J. H. 1975, PhD thesis, Harvard University, Massachusetts
Blandford, R., Simeon, P., & Yuan, Y. 2014, Nuclear Physics B Proceedings Supplements, 256, 9
Blandford, R. D. & Ostriker, J. P. 1978, ApJ, 221, L29
Blasi, P. 2013, A&A Rev., 21, 70
Blumenthal, G. R. & Gould, R. J. 1970, Reviews of Modern Physics, 42, 237
Bovino, S., Ferrada-Chamorro, S., Lupi, A., Schleicher, D. R. G., & Caselli, P. 2020, MNRAS, 495, L7
Bracco, A., Ntormousi, E., Jelić, V., et al. 2022, arXiv e-prints, arXiv:2204.02774
Brunger, M. J., Buckman, S. J., & Newman, D. S. 1990, Australian Journal of Physics, 43, 665
Brunger, M. J., Buckman, S. J., Newman, D. S., & Alle, D. T. 1991, Journal of Physics B Atomic Molecular Physics, 24, 1435
Casandjian, J.-M. 2015, ApJ, 806, 240
Caselli, P., Walmsley, C. M., Terzieva, R., & Herbst, E. 1998, ApJ, 499, 234
Ceccarelli, C., Dominik, C., Lefloch, B., Caselli, P., & Caux, E. 2004, ApJ, 607, L51
Ceccarelli, C., Dominik, C., López-Sepulcre, A., et al. 2014, ApJ, 790, L1
Ceccarelli, C., Hily-Blant, P., Montmerle, T., et al. 2011, ApJ, 740, L4
Cleeves, L. I., Adams, F. C., & Bergin, E. A. 2013, ApJ, 772, 5
Cleeves, L. I., Bergin, E. A., Qi, C., Adams, F. C., & Öberg, K. I. 2015, ApJ, 799, 204
Cravens, T. E. & Dalgarno, A. 1978, ApJ, 219, 750
Cravens, T. E., Victor, G. A., & Dalgarno, A. 1975, Planet. Space Sci., 23, 1059
Crompton, R. W., Elford, M. T., & Jory, R. L. 1967, Australian Journal of Physics, 20, 369
Crompton, R. W., Elford, M. T., & Robertson, A. G. 1970, Australian Journal of Physics, 23, 667
Crutcher, R. M. 2012, ARA&A, 50, 29
Crutcher, R. M., Troland, T. H., Lazareff, B., & Kazes, I. 1996, ApJ, 456, 217
Cummings, A. C., Stone, E. C., Heikkila, B. C., et al. 2016, ApJ, 831, 18
Curran, R., Donahue, T. M., & Kasner, W. H. 1959, Physical Review, 114, 490
Dalgarno, A. & Griffing, G. W. 1958, Proceedings of the Royal Society of London Series A, 248, 415
Dalgarno, A., Yan, M., & Liu, W. 1999, ApJS, 125, 237
de Boisanger, C., Helmich, F. P., & van Dishoeck, E. F. 1996, A&A, 310, 315
de Heer, F. J. 1998, Critically assessed electron-impact excitation cross sections for He(1^1S), INDC(NDS)-385, Nuclear Data Section, IAEA, Vienna
De Heer, F. J., Schutten, J., & Moustafa, H. 1966, Physica, 32, 1766
De La Torre Luque, P., Mazziotta, M. N., Loparco, F., Gargano, F., & Serini, D. 2021, J. Cosmology Astropart. Phys., 2021, 099
Dimitriou, K., Aumayr, F., Katsonis, K., & Winter, H. P. 2004, International Journal of Mass Spectrometry, 233, 137
Dodd, J. G. & Hughes, R. H. 1964, Physical Review, 135, 618
Dogiel, V. A., Chernyshov, D. O., Kiselev, A. M., et al. 2015, ApJ, 809, 48
Drury, L. O. 1983, Reports on Progress in Physics, 46, 973
Edgar, B. C., Miles, W. T., & Green, A. E. S. 1973, J. Geophys. Res., 78, 6595
Edgar, B. C., Porter, H. S., & Green, A. E. S. 1975, Planet. Space Sci., 23, 787
Ehrhardt, H., Langhans, L., Linder, F., & Taylor, H. S. 1968, Physical Review, 173, 222

England, J. P., Elford, M. T., & Crompton, R. W. 1988, Australian Journal of Physics, 41, 573
Errea, L. F., Illescas, C., Macías, A., et al. 2010, J. Chem. Phys., 133, 244307
Erskine, G. A. 1954, Proceedings of the Royal Society of London Series A, 224, 362
Evoli, C., Morlino, G., Blasi, P., & Aloisio, R. 2020, Phys. Rev. D, 101, 023013
Favre, C., Ceccarelli, C., López-Sepulcre, A., et al. 2018, ApJ, 859, 136
Fermi, E. 1949, Physical Review, 75, 1169
Fermi, E. 1954, ApJ, 119, 1
Fitz Axen, M., Offner, S. S. S., Gaches, B. A. L., et al. 2021, ApJ, 915, 43
Fontani, F., Ceccarelli, C., Favre, C., et al. 2017, A&A, 605, A57
Fraschetti, F., Drake, J. J., Cohen, O., & Garraffo, C. 2018, ApJ, 853, 112
Fritsch, W. 1991, Physics Letters A, 160, 64
Fuente, A., Cernicharo, J., Roueff, E., et al. 2016, A&A, 593, A94
Fujii, Y. I. & Kimura, S. S. 2022, ApJ, 937, L37
Fursa, D. V. & Bray, I. 2003, Journal of Physics B Atomic Molecular Physics, 36, 1663
Gabici, S. 2011, in Cosmic Rays for Particle and Astroparticle Physics, ed. S. Giani, C. Leroy, & P. G. Rancoita, 343–351
Gaches, B. A. L., Bialy, S., Bisbas, T. G., et al. 2022, A&A, 664, A150
Gaches, B. A. L. & Offner, S. S. R. 2018, ApJ, 861, 87
Gaches, B. A. L., Offner, S. S. R., & Bisbas, T. G. 2019, ApJ, 878, 105
Garcia, J. D., Gerjuoy, E., & Welker, J. E. 1968, Physical Review, 165, 66
Gealy, M. W. & van Zyl, B. 1987, Phys. Rev. A, 36, 3100
Gentry, W. R. & Giese, C. F. 1975, Phys. Rev. A, 11, 90
Gianturco, F. A. & Tritella, P. 1977, Phys. Rev. A, 16, 542
Gilbody, H. B. & Hasted, J. B. 1957, Proceedings of the Royal Society of London Series A, 240, 382
Ginzburg, V. L. & Syrovatskii, S. I. 1964, The Origin of Cosmic Rays
Ginzburg, V. L. & Syrovatskii, S. I. 1965, ARA&A, 3, 297
Girart, J. M., Beltrán, M. T., Zhang, Q., Rao, R., & Estalella, R. 2009, Science, 324, 1408
Glassgold, A. E. & Langer, W. D. 1974, ApJ, 193, 73
Gloeckler, G. & Fisk, L. A. 2015, ApJ, 806, L27
Goldreich, P. & Kylafis, N. D. 1981, ApJ, 243, L75
Grassi, T., Padovani, M., Ramsey, J. P., et al. 2019, MNRAS, 484, 161
Gredel, R. & Dalgarno, A. 1995, ApJ, 446, 852
Gredel, R., Lepp, S., Dalgarno, A., & Herbst, E. 1989, ApJ, 347, 289
Grenier, I. A., Black, J. H., & Strong, A. W. 2015, ARA&A, 53, 199
Hall, R. I. & Andric, L. 1984, Journal of Physics B Atomic Molecular Physics, 17, 3815
Hargreaves, L. R., Bhari, S., Adjari, B., et al. 2017, Journal of Physics B Atomic Molecular Physics, 50, 225203
Heays, A. N., Bosman, A. D., & van Dishoeck, E. F. 2017, A&A, 602, A105
Hennebelle, P. & Ciardi, A. 2009, A&A, 506, L29
Herrero, F. A. & Doering, J. P. 1972, Phys. Rev. A, 5, 702
Hezareh, T., Houde, M., McCoey, C., Vastel, C., & Peng, R. 2008, ApJ, 684, 1221
Hollenbach, D., Kaufman, M. J., Neufeld, D., Wolfire, M., & Goicoechea, J. R. 2012, ApJ, 754, 105
Indriolo, N., Bergin, E. A., Falgarone, E., et al. 2018, ApJ, 865, 127
Indriolo, N., Blake, G. A., Goto, M., et al. 2010, ApJ, 724, 1357
Indriolo, N. & McCall, B. J. 2012, ApJ, 745, 91
Indriolo, N., Neufeld, D. A., Gerin, M., et al. 2015, ApJ, 800, 40
Ivlev, A. V., Padovani, M., Galli, D., & Caselli, P. 2015, ApJ, 812, 135

Ivlev, A. V., Silsbee, K., Padovani, M., & Galli, D. 2021, ApJ, 909, 107
Janev, R. K., Reiter, D., & Samm, U. 2003, Collision Processes in Low-Temperature Hydrogen Plasmas, (Jülich, Germany: Forschungszentrum, Zentralbibliothek)
Joos, M., Hennebelle, P., & Ciardi, A. 2012, A&A, 543, A128
Kato, H., Kawahara, H., Hoshino, M., et al. 2008, Phys. Rev. A, 77, 062708
Kato, T., Itikawa, Y., & Sakimoto, K. 1992, Compilation of excitation cross sections for He atoms by electron impact, NIFS-DATA-15, NIFS, Nagoya
Khakoo, M. A. & Segura, J. 1994, Journal of Physics B Atomic Molecular Physics, 27, 2355
Khakoo, M. A. & Trajmar, S. 1986, Phys. Rev. A, 34, 146
Khakoo, M. A., Trajmar, S., McAdams, R., & Shyn, T. W. 1987, Phys. Rev. A, 35, 2832
Kim, Y.-K., Santos, J. P., & Parente, F. 2000, Phys. Rev. A, 62, 052710
Knipp, J. K., Eguchi, T., Ohta, M., & Nagata, S. 1953, Progress of Theoretical Physics, 10, 24
Krakau, S. & Schlickeiser, R. 2015, ApJ, 802, 114
Krause, J., Morlino, G., & Gabici, S. 2015, in International Cosmic Ray Conference, Vol. 34, 34th International Cosmic Ray Conference (ICRC2015), 518
Krstić, P. S. & Schultz, D. R. 1999, Phys. Rev. A, 60, 2118
Krymskii, G. F. 1977, Akademiia Nauk SSSR Doklady, 234, 1306
Lazarian, A. & Xu, S. 2021, ApJ, 923, 53
Lazarian, A. & Yan, H. 2014, ApJ, 784, 38
Le Petit, F., Ruaud, M., Bron, E., et al. 2016, A&A, 585, A105
Linder, F. 1980, in Proceedings of the XIth International Conference on the Physics of Electronic and Atomic Collisions, ed. N. Oda & L. Takayanagi, 535
Linder, F. & Schmidt, H. 1971, Zeitschrift Naturforschung Teil A, 26, 1603
Liu, X., Shemansky, D. E., Yoshii, J., et al. 2017, ApJS, 232, 19
Longair, M. S. 2011, High Energy Astrophysics
Luo, G., Zhang, Z.-Y., Bisbas, T. G., et al. 2022, arXiv e-prints, arXiv:2211.13380
Mannheim, K. & Schlickeiser, R. 1994, A&A, 286, 983
Maret, S. & Bergin, E. A. 2007, ApJ, 664, 956
Mason, N. J. & Newell, W. R. 1986, Journal of Physics B Atomic Molecular Physics, 19, L587
McCall, B. J., Hinkle, K. H., Geballe, T. R., et al. 2002, ApJ, 567, 391
McCall, B. J., Huneycutt, A. J., Saykally, R. J., et al. 2003, Nature, 422, 500
McElroy, D., Walsh, C., Markwick, A. J., et al. 2013, A&A, 550, A36
Melrose, D. B. 2009, arXiv e-prints, arXiv:0902.1803
Merabet, H., Bailey, M., Bruch, R., et al. 2001, Phys. Rev. A, 64, 012712
Miller, J. H. & Green, A. E. S. 1973, Radiation Research, 54, 343
Milloy, H. B. & Crompton, R. W. 1977, Phys. Rev. A, 15, 1847
Morales Ortiz, J. L., Ceccarelli, C., Lis, D. C., et al. 2014, A&A, 563, A127
Moskalenko, I. V. & Mashnik, S. G. 2003, in International Cosmic Ray Conference, Vol. 4, International Cosmic Ray Conference, 1969
Neufeld, D. A., Goicoechea, J. R., Sonnentrucker, P., et al. 2010, A&A, 521, L10
Neufeld, D. A. & Wolfire, M. G. 2017, ApJ, 845, 163
Niedner, G., Noll, M., Toennies, J. P., & Schlier, C. 1987, J. Chem. Phys., 87, 2685
Nishimura, H. & Danjo, A. 1986, Journal of the Physical Society of Japan, 55, 3031
Nishimura, H., Danjo, A., & Sugahara, H. 1985, Journal of the Physical Society of Japan, 54, 1757
O'Donoghue, R., Viti, S., Padovani, M., & James, T. 2022, ApJ, 934, 63
Orlando, E. 2018, MNRAS, 475, 2724
Owen, E. R., On, A. Y. L., Lai, S.-P., & Wu, K. 2021, ApJ, 913, 52
Padovani, M., Bialy, S., Galli, D., et al. 2022, arXiv e-prints, arXiv:2201.08457

Padovani, M., Bracco, A., Jelić, V., Galli, D., & Bellomi, E. 2021a, A&A, 651, A116
Padovani, M. & Galli, D. 2018, A&A, 620, L4
Padovani, M., Galli, D., & Glassgold, A. E. 2009, A&A, 501, 619
Padovani, M., Galli, D., Ivlev, A. V., Caselli, P., & Ferrara, A. 2018a, A&A, 619, A144
Padovani, M., Hennebelle, P., & Galli, D. 2013, A&A, 560, A114
Padovani, M., Hennebelle, P., Marcowith, A., & Ferrière, K. 2015, A&A, 582, L13
Padovani, M., Ivlev, A. V., Galli, D., & Caselli, P. 2018b, A&A, 614, A111
Padovani, M., Ivlev, A. V., Galli, D., & Caselli, P. 2018c, A&A, 614, A111
Padovani, M., Marcowith, A., Galli, D., Hunt, L. K., & Fontani, F. 2021b, A&A, 649, A149
Padovani, M., Marcowith, A., Hennebelle, P., & Ferrière, K. 2016, A&A, 590, A8
Padovani, M., Marcowith, A., Sánchez-Monge, Á., Meng, F., & Schilke, P. 2019, A&A, 630, A72
Phan, V. H. M., Schulze, F., Mertsch, P., Recchia, S., & Gabici, S. 2021, Phys. Rev. Lett., 127, 141101
Phelps, A. V. 1990, J. Phys. Chem. Ref. Data, 19, 653
Pinto, C. & Galli, D. 2008, A&A, 484, 17
Podio, L., Lefloch, B., Ceccarelli, C., Codella, C., & Bachiller, R. 2014, A&A, 565, A64
Prasad, S. S. & Tarafdar, S. P. 1983, ApJ, 267, 603
Rab, C., Güdel, M., Padovani, M., et al. 2017, A&A, 603, A96
Ralchenko, Yu., Janev, R. K., Kato, T., et al. 2008, Atomic Data and Nuclear Data Tables, 94, 603
Ramanan, G. & Freeman, G. R. 1990, J. Chem. Phys., 93, 3120
Redaelli, E., Sipilä, O., Padovani, M., et al. 2021, A&A, 656, A109
Rimmer, P. B., Herbst, E., Morata, O., & Roueff, E. 2012, A&A, 537, A7
Robinson, J. M. & Gilbody, H. B. 1967, Proceedings of the Physical Society, 92, 589
Rodgers-Lee, D., Taylor, A. M., Downes, T. P., & Ray, T. P. 2020, MNRAS, 491, 4742
Rodgers-Lee, D., Taylor, A. M., Ray, T. P., & Downes, T. P. 2017, MNRAS, 472, 26
Rodríguez, V. D., Ramírez, C. A., Rivarola, R. D., & Miraglia, J. E. 1997, Phys. Rev. A, 55, 4201
Rudd, M. E. 1988, Phys. Rev. A, 38, 6129
Rudd, M. E. 1991, Phys. Rev. A, 44, 1644
Rudd, M. E., Goffe, T. V., Dubois, R. D., Toburen, L. H., & Ratcliffe, C. A. 1983, Phys. Rev. A, 28, 3244
Rudd, M. E., Kim, Y. K., Madison, D. H., & Gallagher, J. W. 1985, Reviews of Modern Physics, 57, 965
Sabatini, G., Bovino, S., Giannetti, A., et al. 2020, A&A, 644, A34
Sanhueza, P., Girart, J. M., Padovani, M., et al. 2021, ApJ, 915, L10
Scarlett, L. H., Fursa, D. V., Zammit, M. C., et al. 2021, Atomic Data and Nuclear Data Tables, 137, 101361
Scarlett, L. H., Tapley, J. K., Savage, J. S., et al. 2019, Plasma Sources Science Technology, 28, 025004
Schilke, P., Neufeld, D. A., Müller, H. S. P., et al. 2014, A&A, 566, A29
Schinke, R. 1977, Chemical Physics, 24, 379
Schlickeiser, R. 2002, Cosmic Ray Astrophysics
Schlickeiser, R. 2015, Physics of Plasmas, 22, 091502
Schmidt, B., Berkhan, K., Götz, B., & Müller, M. 1994, Physica Scripta Volume T, 53, 30
Schure, K. M., Bell, A. R., O'C Drury, L., & Bykov, A. M. 2012, Space Sci. Rev., 173, 491
Shaw, G., Ferland, G. J., Srianand, R., et al. 2008, ApJ, 675, 405
Shyn, T. W. & Sharp, W. E. 1981, Phys. Rev. A, 24, 1734
Silsbee, K. & Ivlev, A. V. 2019, ApJ, 879, 14
Skilling, J. 1975, MNRAS, 173, 255

Spencer, L. V. & Fano, U. 1954, Physical Review, 93, 1172
Stier, P. M. & Barnett, C. F. 1956, Physical Review, 103, 896
Stone, E. C., Cummings, A. C., Heikkila, B. C., & Lal, N. 2019, Nature Astronomy, 3, 1013
Strong, A. & Fermi-LAT Collaboration. 2015, in International Cosmic Ray Conference, Vol. 34, 34th International Cosmic Ray Conference (ICRC2015), 506
Strong, A. W., Moskalenko, I. V., & Ptuskin, V. S. 2007, Annual Review of Nuclear and Particle Science, 57, 285
Swartz, W. E., Nisbet, J. S., & Green, A. E. S. 1971, J. Geophys. Res., 76, 8425
Syrovatsky, S. I. 1970, in International Cosmic Ray Conference, Vol. 1, International Cosmic Ray Conference, 17
Tabata, T. & Shirai, T. 2000, Atomic Data and Nuclear Data Tables, 76, 1
Takayanagi, K. 1973, PASJ, 25, 327
Thomas, E. W. & Bent, G. D. 1967, Physical Review, 164, 143
Tibaldo, L., Gaggero, D., & Martin, P. 2021, Universe, 7, 141
Toburen, L. H. & Wilson, W. E. 1972, Phys. Rev. A, 5, 247
Uhlmann, L. J., dall, R. G., Truscott, A. G., et al. 2005, Phys. Rev. Lett., 94, 173201
Umebayashi, T. & Nakano, T. 1981, PASJ, 33, 617
Van den Bos, J., Winter, G. J., & De Heer, F. J. 1968, Physica, 40, 357
van der Tak, F. F. S. & van Dishoeck, E. F. 2000, A&A, 358, L79
Van Eck, J., De Heer, F. J., & Kistemaker, J. 1964, Physica, 30, 1171
van Zyl, B., Gealy, M. W., & Neumann, H. 1989, Phys. Rev. A, 40, 1664
van Zyl, B., Jaecks, D., Pretzer, D., & Geballe, R. 1967, Physical Review, 158, 29
van Zyl, B., Le, T. Q., & Amme, R. C. 1981, J. Chem. Phys., 74, 314
Vaupré, S., Hily-Blant, P., Ceccarelli, C., et al. 2014, A&A, 568, A50
Vlemmings, W. H. T., Humphreys, E. M. L., & Franco-Hernández, R. 2011, ApJ, 728, 149
Vriens, L. 1967, Physical Review, 160, 100
Šternberg, Z. & Tomaš, P. 1961, Physical Review, 124, 810
Wakelam, V., Loison, J. C., Herbst, E., et al. 2015, ApJS, 217, 20
Welsheit, J. C. 1973, ApJ, 185, 877
Williams, I. D., Geddes, J., & Gilbody, H. B. 1982, Journal of Physics B Atomic Molecular Physics, 15, 1377
Wolleben, M. & Reich, W. 2004, A&A, 427, 537
Wrkich, J., Mathews, D., Kanik, I., Trajmar, S., & Khakoo, M. A. 2002, Journal of Physics B Atomic Molecular Physics, 35, 4695
Xu, Y. & McCray, R. 1991, ApJ, 375, 190
Yan, H. & Lazarian, A. 2004, ApJ, 614, 757
Yoon, J.-S., Song, M.-Y., Han, J.-M., et al. 2008, Journal of Physical and Chemical Reference Data, 37, 913
Zawadzki, M., Wright, R., Dolmat, G., et al. 2018, Phys. Rev. A, 98, 062704
Zweibel, E. G. 2013, Physics of Plasmas, 20, 055501